https://doi.org/10.26599/FRICT.2026.9441333

Research Article

Mechanism of AC current transmission across rough contact interfaces

Aizhong Liao[1, 2, 3], Wurui Ta[1, 2, 3, *], Youhe Zhou[1, 2, 3]

[1] Institute of Superconductor Mechanics, Lanzhou University, Lanzhou 730000, China

[2] Department of Mechanics and Engineering Science, College of Civil Engineering and Mechanics, Lanzhou University, Lanzhou 730000, China

[3] Key Laboratory of Mechanics on Environment and Disaster in Western China, Ministry of Education of China, Lanzhou University, Lanzhou 730000, China

* Corresponding authors: tawr@lzu.edu.cn

Received: June 28, 2026; Revised: August 14, 2026; Accepted: October 29, 2026

© The Author(s) 2026.

Just Accepted

Abstract

The transmission mechanism of high-frequency alternating current (AC) across rough contact interfaces is a key issue in the design and performance evaluation of connectors, relays, current-collection systems, and advanced electronic and energy devices. Under AC excitation, conductive transport occurs through real contact regions, while capacitance forms naturally across non-contact gaps. These two effects jointly

govern the broadband impedance response of the interface. However, this mechanism is affected by surface roughness, normal load, skin effect, electromagnetic diffusion in the substrate, and the electrical boundary condition at the backside of the substrate. This study establishes a load-dependent resistance-capacitance model to quantify the dependence of contact resistance and gap capacitance on load, and reveals how load and frequency affect the competition between conductive transport through contact spots and displacement-current transport across non-contact gaps. The conductive formulation is quantitatively verified against Holm's DC solution and Bowler's finite-frequency analytical solution, with maximum deviations below 3.115% and 0.081%, respectively. The effects of surface roughness, skin effect, conductor thickness, and backside electrical boundary conditions on the interfacial impedance response are further examined. The broadband complex impedance is also investigated as a load-sensitive electrical signature of the rough contact state under measurement uncertainty. This study provides a numerical framework for interpreting the load- and frequency-dependent AC impedance response of rough electrical contact interfaces.

Keywords: rough interface, AC current transmission, contact resistance, gap capacitance, skin effect

Just Accepted

1. Introduction

Contact interfaces are widespread in connectors, relays, switches, current-collection systems, and advanced electronic and energy devices [1,2,3]. The current conduction behavior across these interfaces directly determines the performance of electrical contact devices. As electronic systems move toward higher frequencies,

broader bandwidths, and higher speeds, such as in 5G/6G RF connections, high-speed interconnects, advanced packaging, and high-frequency power devices, contact interfaces are subjected to increasing high-frequency alternating current (AC) excitation [4,5,6]. Therefore, revealing how rough contact interfaces govern the transmission of high-frequency AC current under loading is a key issue in the design and performance evaluation of electrical contact devices.

It is well known that, because of the randomness and complex distribution of solid surface roughness, the real contact area at a contact interface is much smaller than the nominal contact area. Under loading, the random contact between different asperities and the unsynchronized deformation of these asperities make the changes in contact area and contact gap strongly nonlinear. Under direct current (DC), the current constricts sharply at the interface, which generates contact resistance in the contact region that is higher than the bulk resistance and thus hinders current flow [7,8,9,10]. Under AC excitation, the situation becomes more complex. In addition to the contact resistance in the contact region, capacitance naturally forms across the non-contact gaps, and displacement current also arises [9,11,12,13]. In addition, the skin effect, electromagnetic diffusion, and the boundary features of the bulk all affect the current transmission behavior at the contact interface. Therefore, it is necessary to systematically consider the effect of loading on the contact area and contact gap, and then establish the broadband complex impedance characteristics that include bulk resistance, interfacial resistance, gap capacitance, and displacement current [4,5,6,11,14,15]. Only in this way can the mechanism by which the contact interface

Just Accepted

affects AC transport under the combined effects of loading, interface geometry, and current transmission be clarified.

Existing studies related to electrical transport across rough interfaces can be grouped into three main aspects. The first aspect concerns contact resistance and conductive transport through real contact spots. Holm's classical theory gives the constriction resistance associated with current transport through micro-contact spots and lays the foundation for the study of contact resistance [9]. Timsit summarized the characteristics of electrical contact resistance at stationary interfaces and discussed the effects of interfacial films, surface condition, and contact state [16]. For rough elastic contacts, Barber established important relations between contact conductance, contact stiffness, and rough-surface contact mechanics [17,18]. Yastrebov et al. examined the representativeness of rough-surface contact simulations and the evolution of true contact area from infinitesimal to nearly full contact [15,19]. They also developed a three-level multiscale model for electrical contacts and compared the numerical predictions with experimental measurements [20]. In addition, Jackson et al. extended rough-surface electrical contact resistance models by considering scale-dependent material properties and quantum effects at small asperity contacts [21]. Recent numerical models have further included asperity interaction, elastoplastic deformation, and multi-physics coupling, thereby improving the prediction of electrical contact resistance for rough interfaces [22,23,24].

A second relevant line of work concerns capacitance, local electric-field enhancement, and dielectric response in rough gaps or rough insulating films. For non-

Just Accepted

contacting regions, the local electric field is affected not only by the mean separation but also by the detailed surface geometry. Zhao et al. showed that surface roughness can change the electric field, capacitance, and leakage current of insulating films [25]. Bruce et al. further analyzed the capacitance of rough-surface capacitors and proposed approximate expressions for different roughness regimes [26]. From another viewpoint, Fosco et al. developed an improved proximity-force approximation for electrostatics based on a derivative expansion of the electrostatic energy. Their result shows that, for a gently varying conducting surface facing a plane, the first slope correction to the local parallel-plate energy has a universal coefficient of 1/3 [27]. More recently, Torabi et al. showed that realistic rough electrodes can produce excess capacitance in thin-film capacitors compared with the classical parallel-plate prediction [28]. These studies indicate that the local parallel-plate formula should not be interpreted as an exact capacitance for a rough gap. Local slope, curvature, and near-contact geometric features can induce lateral electric-field components and local field enhancement, which may change the effective capacitance. In addition, dielectric breakdown in narrow interfacial gaps has recently been incorporated into electrical-contact models and electrified elastohydrodynamic line-contact models [29,30]. Related studies on lubricated contacts also show that surface asperities can enhance micro electrical discharge [31]. These studies suggest that a purely capacitive dielectric description has a limited range of validity when the local electric field becomes sufficiently high. This treatment provides a reduced-order dielectric response before breakdown and clarifies the relation between the parallel-plate approximation, roughness-induced slope correction, and the full

Just Accepted

electrostatic solution.

The third category concerns AC current behavior. Timsit pointed out that passive contact elements in high-speed connectors cannot be treated simply as static conducting units, and that their high-frequency response should be analyzed from the viewpoint of electromagnetic propagation and transmission-line behavior [4]. From the viewpoint of interfacial electromechanical coupling, Zhai et al. showed that changes in contact state affect both interfacial conduction and dielectric response [13]. Wang et al. further investigated the stress-dependent impedance behavior of fractal rough interfaces and showed that both the interfacial capacitance and the characteristic frequency evolve with the applied load [12]. Dayan et al. showed in their study of passive intermodulation in rough conductor contacts that contact nonlinearity under high-frequency conditions significantly affects radio-frequency signal quality [11]. Zhou et al. further demonstrated that microscale surface roughness can change AC contact impedance and signal transmission in radio-frequency coaxial connectors [6].

These studies explain the variation of contact resistance with load under DC current and establish the relationship between interfacial capacitance and characteristic frequency. However, many existing studies still treat direct-current and AC current cases separately and do not provide broadband complex impedance characteristics that include contact resistance, gap capacitance, displacement current, and skin effect in a unified load-dependent framework. As a result, the competition and transition between conductive transport through real contact spots and displacement-current transport across non-contact gaps remain insufficiently clarified under AC excitation. Meanwhile,

Just Accepted

because of the complexity of interfacial roughness, existing contact-resistance calculations usually consider the load-dependent variation of real contact area, whereas the corresponding variation of interfacial capacitance caused by the load-dependent gap field has received less attention. Consequently, it is difficult to accurately characterize the influence of normal load on the broadband electrical response of rough contact interfaces.

On this basis, this paper considers the variations in contact gap, contact resistance, displacement current, and skin effect during interfacial contact under loading, and provides a characterization of broadband complex impedance. It then establishes a load-dependent resistance-capacitance model and reveals the mechanism by which rough contact interfaces govern high-frequency AC transport. The effects of surface roughness, finite-thickness propagation, and backside electrical boundary conditions are further examined. The broadband impedance spectrum is finally discussed as a load-sensitive electrical signature of the rough contact state under measurement uncertainty. The rest of this paper is organized as follows. Section 2 presents the theoretical model. Section 3 provides model validation and comparison. Section 4 presents the main results. Section 5 provides a brief discussion. Section 6 concludes the paper.

2. Theoretical model

To systematically describe the mechanism by which the contact interface affects AC transport, three aspects need to be analyzed: the contact state and gap distribution of the interface under load, the current transport characteristics in the bulk and interfacial regions, and the displacement-current transport characteristics across the

Just Accepted

gaps. Therefore, this section first uses contact mechanics analysis to determine the real contact state and the distribution of non-contact gaps, which provide the geometric input for the subsequent electrical solution. It then establishes a spectral-domain surface-impedance representation for the conductive branch based on the frequency-domain Maxwell equations, which is used to describe electrical conduction in the contact regions and dispersive propagation in the bulk. Finally, the gaps in the non-contact regions are closed into capacitive channels and are coupled in parallel with the conductive branches in the contact regions, thereby yielding the total complex impedance of the rough interface.

2.1 Interfacial Contact State and Gap Distribution

We consider the contact between a rigid rough indenter and a deformable conducting substrate under AC excitation, as shown in Fig. 1(a, b).

Just Accepted

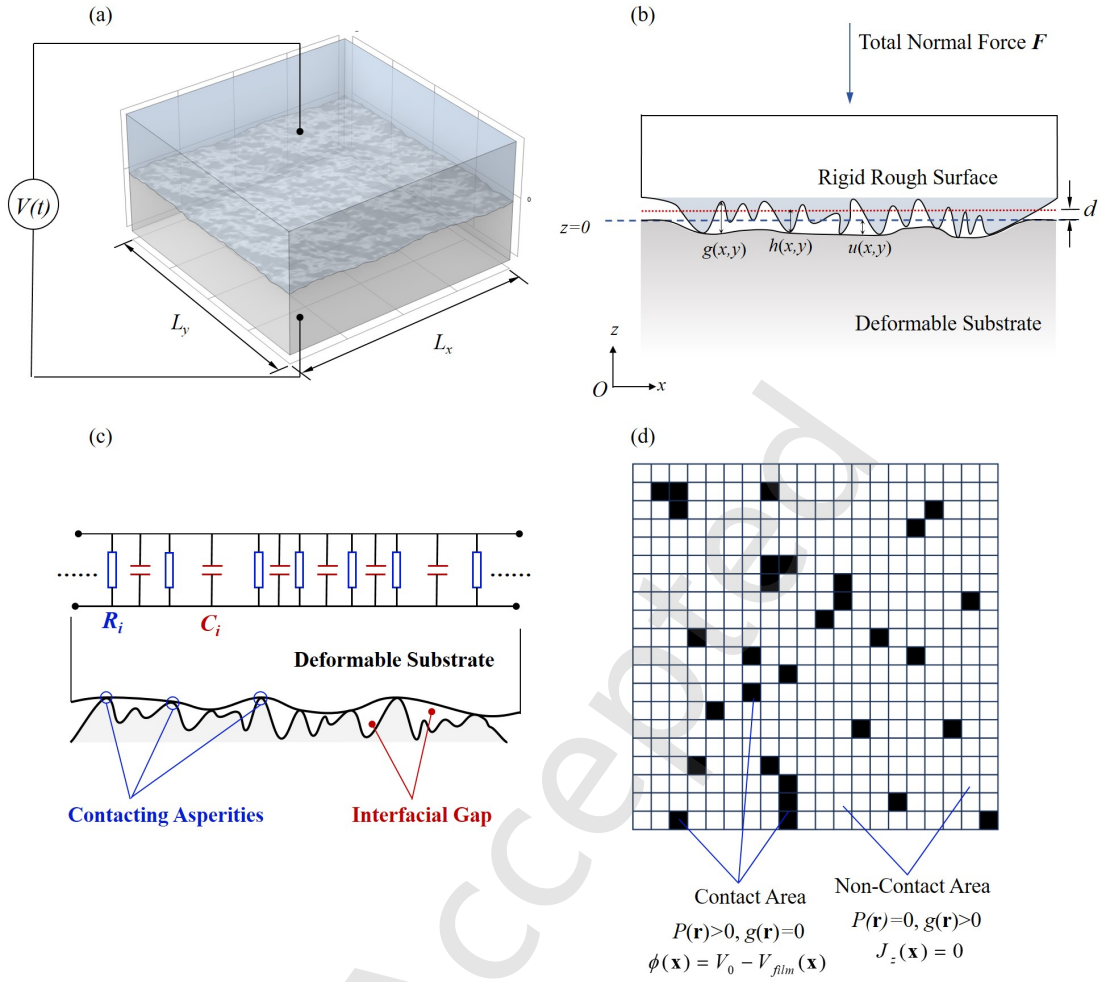


Fig. 1. Physical model and equivalent interfacial electrical model of rough-surface electrical contact under AC excitation: (a) three-dimensional schematic of the nominal contact region under an applied alternating-voltage difference; (b) cross-sectional configuration of a rigid rough indenter and a deformable conducting substrate under normal load; (c) schematic of the parallel conductive-capacitive branch formed jointly by real contact asperities and interfacial gaps; and (d) discrete representation of the continuous contact-state indicator on the computational grid, where black and white cells denote contact and non-contact cells, respectively.

The conductive paths across the interface can be represented by a parallel circuit that consists of several current paths between contacting asperities and several paths

Just Accepted

associated with displacement current through the gaps, as shown in Fig. 1(c). When the interface is discretized, the contact and non-contact regions are found to be randomly distributed. The contact regions correspond to conductive boundary conditions, whereas the non-contact regions correspond to the integral boundary condition for gap capacitance, as shown in Fig. 1(d).

Let the nominal contact domain be $\Omega = \left[0, L_x\right] \times \left[0, L_y\right]$, and discretize it with a uniform grid. The height field of the rigid rough surface is denoted by $h(x, y)$ and is taken to have zero mean, the distance from the upper mean plane to the undeformed nominal surface below is d, and the normal displacement of the deformable substrate surface is $u(x, y)$. The local mechanical gap is then defined as

$$g_{\mathrm{m}}(x, y) = d - h(x, y) - u(x, y), \tag{1}$$

where, $g_m = 0$ corresponds to closed contact, whereas $g_m > 0$ corresponds to a non-contact gap. The real contact region is thus defined as

$$\Omega_c = \{(x, y) \in \Omega : g(x, y) = 0\}, \tag{2}$$

and the corresponding contact-state indicator function is

$$m(x, y) = \begin{cases} 1, & (x, y) \in \Omega_c \\ 0, & (x, y) \in \Omega \backslash \Omega_c \end{cases}. \tag{3}$$

In the subsequent electrical model, $m(x, y)$ determines where the conductive boundary condition is imposed, whereas $g(x, y)$ determines the geometric closure of the displacement-current branch in the non-contact region. In the numerical implementation, this continuous indicator function is sampled on a uniform grid; therefore, the rectangular cells in Fig. 1(d) only represent the computational discretization.

Just Accepted

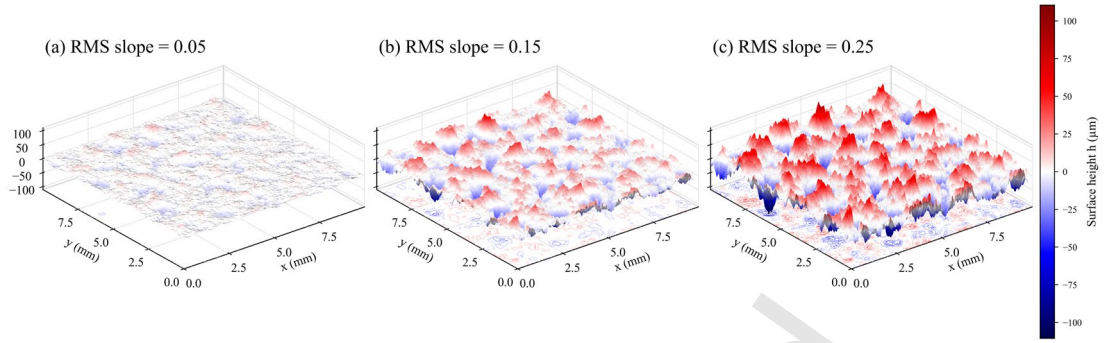


Fig. 2. Representative rough surface topographies generated from an isotropic power-law spectrum at three typical roughness levels (RMS slope = 0.05, 0.15, and 0.25), with all other surface parameters kept constant: $H = 0.8$, $q_0 = q_1 = 4$, and $q_2 = 128$. Here, q_0 is the long-wavelength cutoff, q_1 is the roll-off wavenumber separating the low-wavenumber plateau from the self-affine power-law regime, and q_2 is the short-wavelength cutoff. The indices $L = 10\ mm$, $q_0 = q_1 = 4$ and $q_2 = 128$ correspond to physical wavelengths of 2.5 mm and 78.125 μm, respectively.

In the periodic-surface convention used here, a dimensionless spectral index q_i corresponds to the physical wavelength $\lambda_i = L / q_i$. With L = 10 mm and N = 512, the grid spacing is $\Delta x = \Delta y = L / N = 19.531\ \mu m$. The long-wavelength cutoff and roll-off indices are $q_0 = q_1 = 4$, corresponding to a wavelength of 2.5 mm, whereas the short-wavelength cutoff $q_2 = 128$ corresponds to the shortest retained wavelength of 78.125 μm. The prescribed surface is therefore band-limited and multiscale, rather than a collection of asperities with one intrinsic radius. In the following, the prescribed spectral wavelength range is distinguished from the sizes of the connected contact patches that emerge after deformation.

Under the assumptions of linear elasticity, frictionless contact, and adhesionless

Just Accepted

unilateral contact, the surface displacement and the contact pressure $p(x,y)$ satisfy the linear convolution relation

$$u(\mathbf{r}) = (G * p)(\mathbf{r}) = \int_{\Omega} G(\mathbf{r}-\mathbf{r}')p(\mathbf{r}')dA', \tag{4}$$

where $\mathbf{r} = (x,y)$, and G is the surface Green function of an elastic half-space. For a rigid rough body pressed into an elastic substrate,

$$G(\mathbf{r}-\mathbf{r}') = \frac{1}{\pi E^* |\mathbf{r}-\mathbf{r}'|}, \tag{5}$$

and

$$E^* = \frac{E}{1-\nu^2}. \tag{6}$$

The contact state is determined by the Hertz-Signorini-Moreau complementarity conditions:

$$p(\mathbf{r}) \geq 0, \qquad g_m(\mathbf{r}) \geq 0, \qquad p(\mathbf{r})g_m(\mathbf{r}) = 0. \tag{7}$$

At the same time, the total normal load satisfies the global equilibrium constraint

$$\int_{\Omega} p(\mathbf{r})\,\mathrm{d}\mathbf{r} = F. \tag{8}$$

Let $A_0 = L_x L_y$ denote the nominal contact area, and define the nominal contact pressure as $p_0 = \frac{F}{A_0}$.. Here, p_0 is the total normal load divided by the nominal area and should not be confused with the spatially varying local contact pressure $p(\mathbf{r})$. Unless otherwise stated, the numerical calculations use $L_x = L_y = 10$ mm and hence $A_0 = 100mm^2$. The load interval F=10 – 5000 N therefore corresponds to $p_0 = 0.1 \sim 50$ MPa. This interval specifies the numerical loading range considered in this work; it should not be interpreted as a material-specific elastic range.

For the rigid-rough/elastic-half-space model, the Green function in Eq. (5) is

Just Accepted

proportional to $1/E^*$. Consequently, for a fixed dimensionless topography and Poisson's ratio, the elastic contact solution is governed by the normalized nominal pressure p_0/E^*. At the same nominal pressure, a smaller effective modulus produces larger normal deformation and generally increases the real contact area while reducing the non-contact gaps. These changes affect the subsequent electrical response through two interfacial fields: the contact-state field $m(\mathbf{r})$, which controls the conductive branch, and the deformed gap field $g_m(\mathbf{r})$, which controls the capacitive branch.

By prescribing an isotropic power-law power spectral density, arbitrary rough surface morphologies can be generated, as shown in Fig. 2. Equations (1)–(8) define the load-controlled normal elastic contact subproblem. This subproblem can be solved by standard boundary-element or boundary-integral methods. In the present numerical implementation, Tamaas [32] is used as one such boundary-element solver. The calculation provides the pressure field $p(\mathbf{r})$, the mechanical gap field $g_m(\mathbf{r})$, and the contact-state map $m(\mathbf{r})$. The electrical model derived below uses these interfacial fields as inputs and is not restricted to this particular contact solver or to linear elasticity. Contact masks and gap fields obtained from measured topographies, anisotropic contact models, or material-calibrated elastoplastic calculations can be supplied to the same electrical formulation.

2.2 Spectral surface-impedance formulation

After the contact state and the interfacial gap are obtained, the finite-frequency current response of the substrate is described by the frequency-domain Maxwell equations. For a homogeneous isotropic conductive medium with the time dependence

Just Accepted

$e^{j\omega t}$

$$\nabla \times \mathbf{E} = -j\omega\mu\mathbf{H}, \qquad \nabla \times \mathbf{H} = \hat{\sigma}\mathbf{E}, \qquad \hat{\sigma} = \sigma + j\omega\varepsilon, \tag{9}$$

Here, $\hat{\sigma} = \sigma + j\omega\varepsilon$ is complex conductivity. At finite frequency, the electric field is generally not curl-free; therefore, a three-dimensional scalar electric potential is not introduced. Instead, the surface response is formulated mode by mode in the in-plane Fourier domain. The detailed derivation is given in Appendix A.

Because the material is translationally invariant in the interfacial plane and the numerical implementation uses an in-plane Fourier discretization, a two-dimensional Fourier transform is introduced with the in-plane wave vector $\mathbf{q} = (q_x, q_y)$ and $q = |\mathbf{q}|$. For each nonzero in-plane mode $q > 0$, the normal-current response is described by the transverse-magnetic (TM) spectral component, for which the magnetic field is perpendicular to the $(\mathbf{q}, z)$ plane. The corresponding Maxwell-based derivation is given in Appendix A. We define the spectral surface-potential variable $\hat{\phi}(\mathbf{q}, z)$ through the tangential electric field, $\mathbf{E}_t = -j\mathbf{q}\hat{\phi}$. The Maxwell equations then reduce to

$$\frac{d^2\hat{\phi}}{dz^2} - \Gamma^2\hat{\phi} = 0, \qquad \Gamma^2 = q^2 + j\omega\mu\hat{\sigma} \tag{10}$$

Therefore, each nonzero spectral mode can be treated as an independent one-dimensional propagation problem, and its coefficients are jointly determined by the thickness and the back boundary condition.

Define the spectral-domain surface potential $\hat{\phi}(\mathbf{q})$ and the normal current density $\hat{j}(\mathbf{q})$ in the conductive medium. They satisfy the linear mapping

$$\hat{\phi}(\mathbf{q}) = \hat{K}(\mathbf{q}, \omega)\,\hat{j}(\mathbf{q}), \tag{11}$$

Just Accepted

where $\hat{K}$ is the surface-impedance kernel, which characterizes the potential response at the interface generated by a unit normal current. For a half-space conductor, $\hat{K}$ is uniquely determined by the decay condition in the bulk. For a conductor of finite thickness h_{sub}, the back boundary condition enters in the form of an input impedance. Writing the characteristic impedance as

$$Z_c(q,\omega) = \frac{\Gamma(q,\omega)}{\sigma q^2}, \qquad q > 0. \tag{12}$$

the single-layer surface kernel for common configurations can be written in a unified form as follows: $\hat{K} = Z_c$ for a half-space, $\hat{K} = Z_c \tanh\left(\Gamma h_{sub}\right)$ when the back surface is grounded, and $\hat{K} = Z_c \coth\left(\Gamma h_{sub}\right)$ when the back surface is insulated. If a uniform thin film or a multilayer structure exists on the surface, the total surface kernel can be constructed from bottom to top by the standard input-impedance recursion, and the detailed form is given in Appendix B. In this way, substrate boundary configurations including the half-space case, finite thickness, grounded or insulated back surfaces, and uniform film layers are all considered. The above TM characteristic impedance is defined for $q > 0$. The spatially uniform $q = 0$ component is not obtained by taking the $q \to 0$ limit of Eq. (12), because it depends on the terminal configuration and the global current-closure condition. In the present formulation, the $q = 0$ component is therefore treated separately, as detailed in Appendix B.

For a double-sided contact problem, the total potential difference equals the sum of the surface potential drops on the two sides. Accordingly, the total effective kernel is written as

$$\hat{K}_{\mathrm{eff}}(\mathbf{q},\omega) = \hat{K}_1(\mathbf{q},\omega) + \hat{K}_2(\mathbf{q},\omega). \tag{13}$$

Just Accepted

This expression is formally consistent with the classical Holm series-constriction form, but here the dispersion, skin-effect, and finite-thickness propagation effects are all included in $\hat{K}_{\mathrm{eff}}$. Therefore, the dispersion, skin-effect response, and finite-thickness propagation of current in the bulk are all represented by a nonlocal linear operator relation on the interface,

$$\phi = \mathsf{K}_{\mathrm{eff}}\, j, \tag{14}$$

where $\mathsf{K}_{\mathrm{eff}}$ denotes the complete interfacial operator. Its nonzero-q part is the convolution operator defined by $\hat{K}_{\mathrm{eff}}(q,\omega)$, whereas the spatially uniform component is supplied separately by the global current-closure condition.

This operator, together with the contact-state function $m(\mathbf{r})$, jointly determines the impedance characteristics of the conductive paths formed by asperity contacts. Under the conditions of a half-space, no surface film, the direct-current limit, and single circular-spot contact, this spectral-domain surface-impedance formulation reduces to the contact resistance in the direct-current case, and the result agrees with the classical Holm constriction resistance. The cases of a half-space, finite-thickness conductors with grounded or insulated back electrical boundaries, and double-sided contact are illustrated in Fig. 3.

Just Accepted

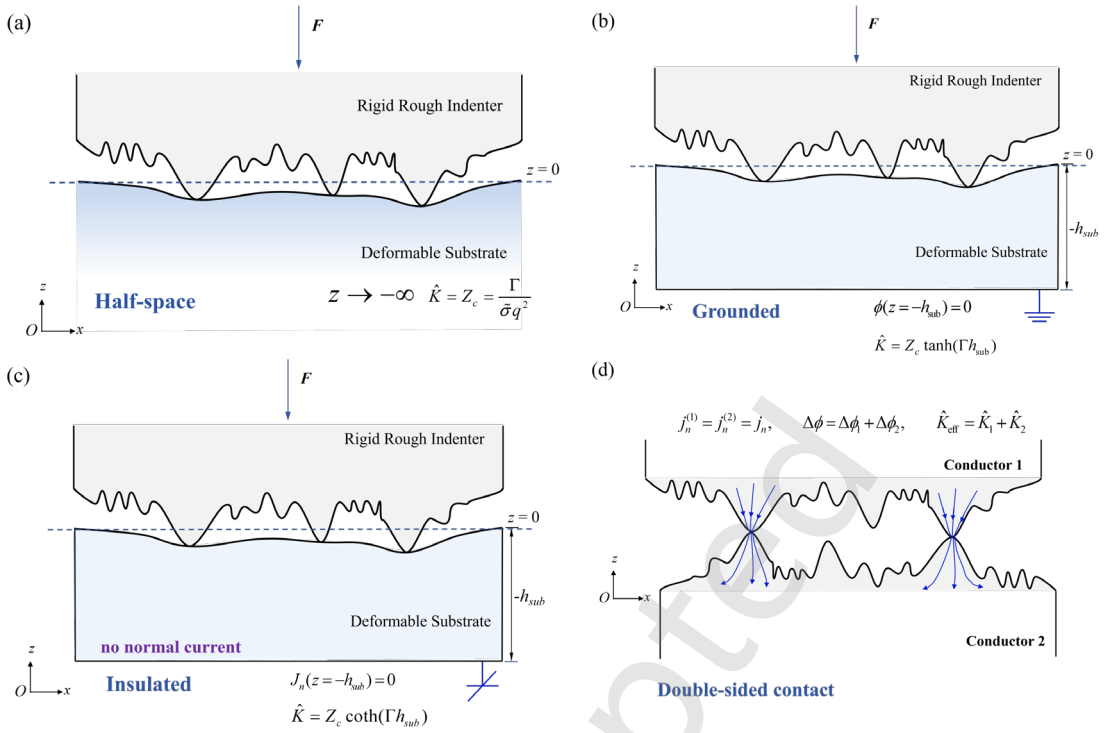


Fig. 3. Schematic illustrations of three different substrate electrical boundary conditions and double-sided contact: (a) single-sided rough contact with a semi-infinite substrate; (b) single-sided rough contact with a grounded electrical boundary condition; (c) single-sided rough contact with an insulated electrical boundary condition; (d) double-sided rough contact between two conductors.

After the surface-impedance kernel has been obtained, the conductive branch is solved only on the true contact region. Let P_c denote the restriction operator from the full interface to Ω_c. Let P_c^T denote the zero-extension operator from Ω_c to the full interface. The contact current density is denoted by j_c. On the contact region, the surface potential is prescribed to be the applied voltage V_0. The boundary conditions in continuous form are

$$\phi(\mathbf{r}) = V_0, \quad \mathbf{r} \in \Omega_c, \tag{15}$$

$$j(\mathbf{r}) = 0, \quad \mathbf{r} \in \Omega, \quad \Omega_c. \tag{16}$$

Just Accepted

Combining these boundary conditions with the surface relation in Eq. (14), the full interfacial current density can be written as $j = P_c^T j_c$, where j_c is the unknown current density on the contact region. Restricting the resulting potential equation back to Ω_c gives the contact-domain equation

$$P_{\mathrm{c}} \mathsf{K}_{\mathrm{eff}} P_{\mathrm{c}}^T j_{\mathrm{c}} = V_0 \mathbf{1}, \tag{17}$$

here, $\mathsf{K}_{\mathrm{eff}}$ is the convolution operator defined by the effective surface-impedance kernel $\hat{K}_{\mathrm{eff}}$. This equation is the discrete mixed boundary-value problem for the conductive branch. The contact region satisfies an equipotential condition. The non-contact region carries no normal conduction current in this branch.

Each matrix-vector product is evaluated by zero-padding the current field, applying a fast Fourier transform, multiplying by $\hat{K}_{\mathbf{eff}}$, and applying the inverse transform before restriction to the contact region. This matrix-free procedure follows the discrete convolution and fast Fourier transform (DC-FFT) method [33]. The resulting linear system is solved using a Krylov method, such as GMRES or BiCGSTAB. Once j_{c} is obtained, the conductive current is

$$I_{\mathrm{cond}} = \int_{\Omega_{\mathrm{c}}} j_{\mathrm{c}}(\mathbf{r}) dA. \tag{18}$$

under the unit-voltage normalization used in this work, the conductive admittance is

$$Y_{\mathrm{cond}}(\omega) = I_{\mathrm{cond}}, \tag{19}$$

for a general applied voltage V_0, it is

$$Y_{\mathrm{cond}}(\omega) = \frac{I_{\mathrm{cond}}}{V_0}. \tag{20}$$

2.3 Variationally bounded capacitive closure of non-contact gaps

In addition to the conductive paths in the true contact regions, the non-contact gaps

Just Accepted

also support displacement current across the interface. They therefore form a capacitive branch. This branch changes both the magnitude and the phase of the interfacial impedance. A detailed variational derivation of the capacitance bounds and their discrete implementation is provided in Appendix C. Here, we summarize the main construction and state the reduced capacitive closure used in the numerical model.

Let Ω_{c} be the true contact region. Let $\Omega_{\mathrm{nc}} = \Omega$, Ω_{c} be the non-contact region. The contact state $m(\mathbf{r})$ and the mechanical gap $g_{\mathrm{m}}(\mathbf{r})$ are obtained from the contact calculation in Section 2.1. In the conductive branch, $m(\mathbf{r})$ determines where the equipotential contact condition is imposed. In the capacitive branch, $g_{\mathrm{m}}(\mathbf{r})$ determines the local dielectric separation in the non-contact region.

We first consider a general rough gap. The two conducting surfaces are written as

$$z = h_1(\mathbf{r}), \qquad z = h_2(\mathbf{r}), \tag{21}$$

where $\mathbf{r} = (x, y)$. The local separation is

$$g(\mathbf{r}) = h_2(\mathbf{r}) - h_1(\mathbf{r}) > 0. \tag{22}$$

The exact capacitance of this rough gap is denoted by C. It is determined by a three-dimensional electrostatic problem. Solving this problem at every load step is expensive. A local parallel-plate formula is much cheaper. However, it is not exact for a rough gap.

The local parallel-plate expression can be interpreted as a variational lower bound. By the Thomson principle,

$$C_{\mathrm{L}} = \varepsilon \int_{\Omega_{\mathrm{nc}}} \frac{1}{g(\mathbf{r})} \mathrm{d}A \le C, \tag{23}$$

where ε is the permittivity of the dielectric medium in the gap. Thus, the local

Just Accepted

parallel-plate formula is not used here as an exact capacitance. It is used as the lower bound of the capacitive branch.

A computable upper bound can be obtained from the Dirichlet principle. We use a trial potential that varies linearly across the local gap. This gives

$$C \le C_{\mathrm{U}}^{\mathrm{lin}} = \varepsilon \int_{\Omega_{\mathrm{nc}}} \frac{1}{g(\mathbf{r})} \left[1 + \frac{|\nabla h_1|^2 + |\nabla h_2|^2 + \nabla h_1 \cdot \nabla h_2}{3} \right] \mathrm{d}A, \tag{24}$$

For a gently varying conducting surface facing a plane, the same 1/3 slope-correction coefficient is obtained from an independent derivative expansion of the electrostatic energy in the improved proximity-force approximation [27]. This agreement indicates that the present Dirichlet upper estimate has the correct second-order slope structure in the smooth non-contact asymptotic limit. Therefore, the capacitance satisfies

$$C_L \le C \le C_{\mathrm{U}}^{\mathrm{lin}}. \tag{25}$$

The difference between $C_{\mathrm{U}}^{\mathrm{lin}}$ and C_{L} is associated with the surface slopes. It measures the additional electrostatic energy introduced by replacing the three-dimensional electric field in a rough gap with a purely one-dimensional local field approximation. When the two surfaces are smooth and parallel, the slope term vanishes. The two bounds then reduce to the classical parallel-plate capacitance. The validity and sharpness of these capacitance bounds are examined by independent finite-element electrostatic benchmarks in Section 3.2.

For the contact problem considered here, the mechanical gap may become very small near contact spots. A dielectric film may also exist in series with the open gap. We therefore define an equivalent series thickness,

Just Accepted

$$t_s = \frac{t_f}{\varepsilon_{r,f}}, \tag{26}$$

where t_f is the film thickness and $\varepsilon_{r,f}$ is the relative permittivity of the film. The film is treated as a spatially uniform and intact equivalent dielectric layer in this reduced closure. The effective gap is then written as

$$G(\mathbf{r}) = g_{\mathrm{m}}(\mathbf{r}) + t_s. \tag{27}$$

A minimum effective gap is also introduced. The regularized gap is

$$G_\tau(\mathbf{r}) = \max\left[G(\mathbf{r}), \tau\right] = \max\left[g_{\mathrm{m}}(\mathbf{r}) + t_s, \tau\right], \tag{28}$$

here, τ represents unresolved near-contact effects. These effects may include nanoscale roughness, tunneling, dielectric breakdown, or finite numerical resolution. The parameter τ should therefore be understood as an effective cutoff for the reduced capacitive closure, rather than as an independently measured material thickness. Under the uniform-film assumption, the minimum effective separation is

$$G_{\mathrm{eff}}^{\min} = \max(t_s, \tau), \tag{29}$$

thus, the cutoff is not controlled by τ alone.

In the numerical implementation of this work, the lower conductor is treated as locally smooth in the capacitive slope correction. The deformation of the substrate is retained in the mechanical gap g_{m}, but its surface slope is not included in the slope correction. The rough upper surface has height $h(\mathbf{r})$. Under this reduced capacitive geometry, the lower and upper estimates become

$$C_{L,\tau} = \varepsilon_0 \int_{\Omega_{nc}} \frac{1}{G_\tau(\mathbf{r})} \mathrm{d}A, \qquad C_{U,\tau}^{\mathrm{lin}} = \varepsilon_0 \int_{\Omega_{nc}} \frac{1}{G_\tau(\mathbf{r})} \left[1 + \frac{|\nabla h(\mathbf{r})|^2}{3}\right] \mathrm{d}A, \tag{30}$$

here, ε_0 is used because the open gap is treated as an air gap, while the film effect has

Just Accepted

already been included through the equivalent series thickness t_s. The upper estimate in Eq. (30) is interpreted under the locally smooth lower-surface approximation stated above.

The baseline capacitance estimate used in the model is taken as the midpoint of these two estimates,

$$\hat{C}_{\mathrm{gap}} = \frac{C_{\mathrm{L}} + C_{\mathrm{U}}^{\mathrm{lin}}}{2}, \tag{31}$$

This gives

$$\hat{C}_{\mathrm{gap}} = \varepsilon_0 \int_{\Omega_{\mathrm{nc}}} \left[\frac{1}{G_\tau(\mathbf{r})} + \frac{|\nabla h(\mathbf{r})|^2}{6 G_\tau(\mathbf{r})} \right] \mathrm{d}A, \tag{32}$$

the first term is the variational lower-bound contribution. The second term is a slope correction inherited from the Dirichlet upper estimate. It accounts for part of the geometric effect of the rough surface. The midpoint value is used as a baseline reduced-order estimate. It should not be interpreted as the exact solution of the full three-dimensional electrostatic problem. The interval between $C_{L,\tau}$ and $C_{U,\tau}^{\mathrm{lin}}$ provides a measure of the uncertainty introduced by the reduced capacitive closure. In the discrete calculation, the integral is evaluated over all non-contact grid cells,

$$\hat{C}_{\mathrm{gap}} = \varepsilon_0 \sum_{(i,j)\in\Omega_{\mathrm{nc}}} \left[\frac{1}{G_{\tau,ij}} + \frac{|\nabla h|_{ij}^2}{6 G_{\tau,ij}} \right] \Delta A. \tag{33}$$

The surface gradient is computed from the same rough surface used in the contact calculation. In the following sections, $\hat{C}_{\mathrm{gap}}$ is denoted simply by C_{gap}, unless the lower and upper estimates are explicitly discussed.

The capacitive admittance is

Just Accepted

$$Y_{\mathrm{gap}}(\omega) = j\omega C_{\mathrm{gap}}, \tag{34}$$

the assembly of this capacitive branch with the conductive branch is described in Section 2.4.

2.4 Assembly of total admittance and computational workflow

The conductive and capacitive branches are assembled at the admittance level. The conductive branch is obtained from the contact-domain mixed boundary-value problem in Section 2.2. The capacitive branch is obtained from the bounded gap closure in Section 2.3. Therefore, the total interfacial admittance is

$$Y_{\mathrm{tot}}(\omega) = Y_{\mathrm{cond}}(\omega) + Y_{\mathrm{gap}}(\omega) = Y_{\mathrm{cond}}(\omega) + j\omega C_{\mathrm{gap}}, \tag{35}$$

the total impedance is

$$Z_{\mathrm{tot}}(\omega) = \frac{1}{Y_{\mathrm{tot}}(\omega)}, \tag{36}$$

This parallel form is a macroscopic assembly rule. It does not mean that the whole interface is a spatially uniform lumped $R \| C$ element. The conductive branch is nonlocal. It is controlled by the contact mask $m(\mathbf{r})$ and the surface-impedance kernel $\hat{K}_{\mathrm{eff}}$. The capacitive branch is controlled by the non-contact gap field $g_{\mathrm{m}}(\mathbf{r})$ and the regularized effective gap $G_r(\mathbf{r})$. The transmission of AC current across the interface is illustrated in Fig. 4.

Just Accepted

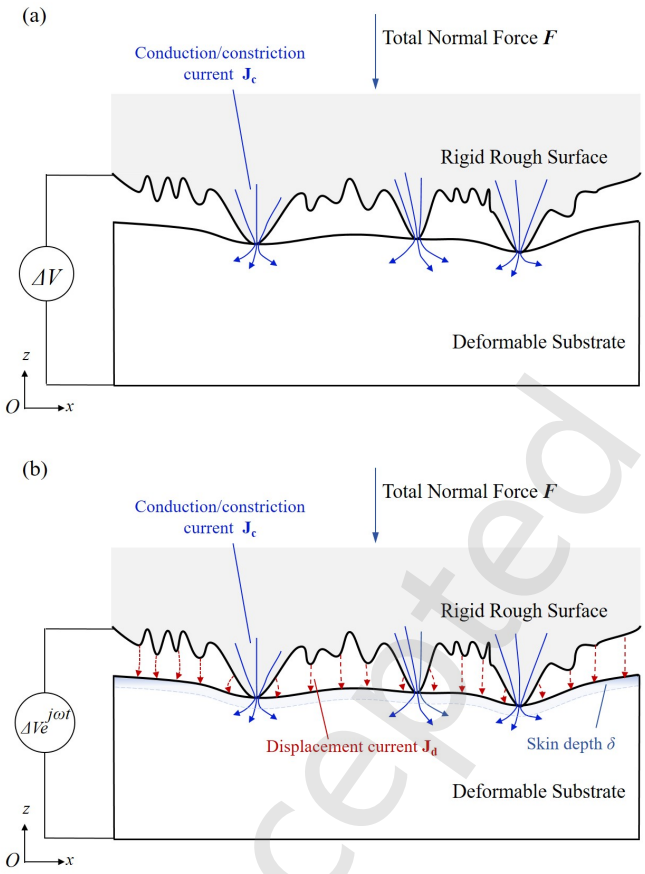


Fig. 4. Schematic illustration of current transport across a rough conductor interface: (a) interfacial current transport under DC excitation; (b) interfacial current transport under AC excitation.

The computational workflow is shown in Fig. 5. First, the rough contact problem is solved under a prescribed normal load F. This step gives the contact pressure $p(\mathbf{r})$, the contact-state map $m(\mathbf{r})$, and the mechanical gap field $g_{\mathrm{m}}(\mathbf{r})$. Second, $m(\mathbf{r})$ is used to define the contact-domain mixed boundary-value problem. The conductive current density $j_{\mathrm{c}}(\mathbf{r})$ is then solved by the DC-FFT surface-impedance operator and a Krylov iterative method. This gives $Y_{\mathrm{cond}}(\omega)$. Third, $g_{\mathrm{m}}(\mathbf{r})$ is used to compute the bounded capacitive closure C_{gap} over Ω_{nc}. This gives $Y_{\mathrm{gap}}(\omega) = j\omega C_{\mathrm{gap}}$. Finally, the two branches are added to obtain $Y_{\mathrm{tot}}(\omega)$ and $Z_{\mathrm{tot}}(\omega)$.

Just Accepted

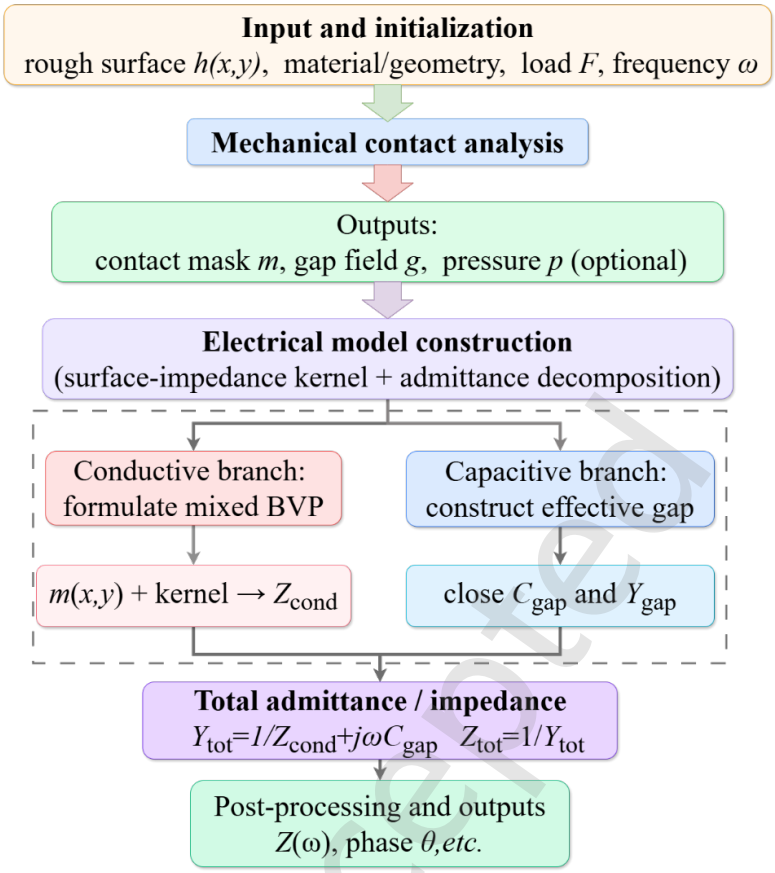


Fig. 5. Computational flow of the method.

This workflow separates the roles of the two geometric outputs from the mechanical contact calculation. The contact map $m(\mathbf{r})$ controls the conductive boundary condition. The gap field $g_{\mathrm{m}}(\mathbf{r})$ controls the capacitive closure. The load dependence of the AC response therefore comes from both the evolution of the true contact region and the evolution of the non-contact gap distribution.

From $Z_{\mathrm{tot}}(\omega)$, the impedance magnitude, phase angle, equivalent resistance, and other frequency-domain response measures can be obtained. These quantities are used in the following sections to analyze the effects of load, roughness, frequency, skin effect, and backside electrical boundary conditions.

Just Accepted

Table 1. Main physical parameters used in the present model (default values)

Parameters	Symbol	Value
Nominal side length of the contact domain	L	10 mm
Poisson's ratio	v	0.30
Elastic modulus	E	100 GPa
Effective elastic modulus	$E^* = E/(1-v^2)$	109.9 GPa
Surface Hurst exponent	H	0.8
Root-mean-square slope	m_{rms}	0.10
Long-wavelength cutoff	q_0	4
Roll-off wavenumber	q_1	4
Short-wavelength cutoff	q_2	128
Substrate conductivity	σ_{sub}	5.998×10^7 S/m
Relative permittivity	$\varepsilon_{r,sub}$	1.0
Relative permeability	$\mu_{r,sub}$	1.0
Uniform thin-film thickness	t_f	100 nm
Conductivity	σ_f	0.01 S/m
Relative permittivity	$\varepsilon_{r,f}$	25
Additional regularization cutoff used for Capacitive closure in the non-contact region	τ	1 nm
Grid resolution	N	512×512

(Note: The default material, roughness, and interfacial-film parameters are mainly adopted from Refs. [12,22] and are used as representative baseline values rather than fitted parameters. The parameter ranges and variations used in the parametric studies are specified in Section 4. The cutoff length τ is introduced for the reduced capacitive closure and is examined separately in Section 4.3.)

3. Verification and model comparison

In this section, the proposed method is examined through comparison with the Holm model, experimental results, and numerical results for the resistance and capacitance responses of rough interfaces under DC and AC conditions. The baseline material, roughness, interfacial-film, and numerical parameters used in the following calculations are summarized in Table 1.

3.1 DC a-spot benchmark

Just Accepted

For the classical case of a single circular asperity contact, the constriction resistance is given by the Holm model as

$$R_{\mathrm{Holm}} = \frac{\rho}{2a}, \tag{37}$$

where ρ is the bulk resistivity and a is the radius of the circular contact spot.

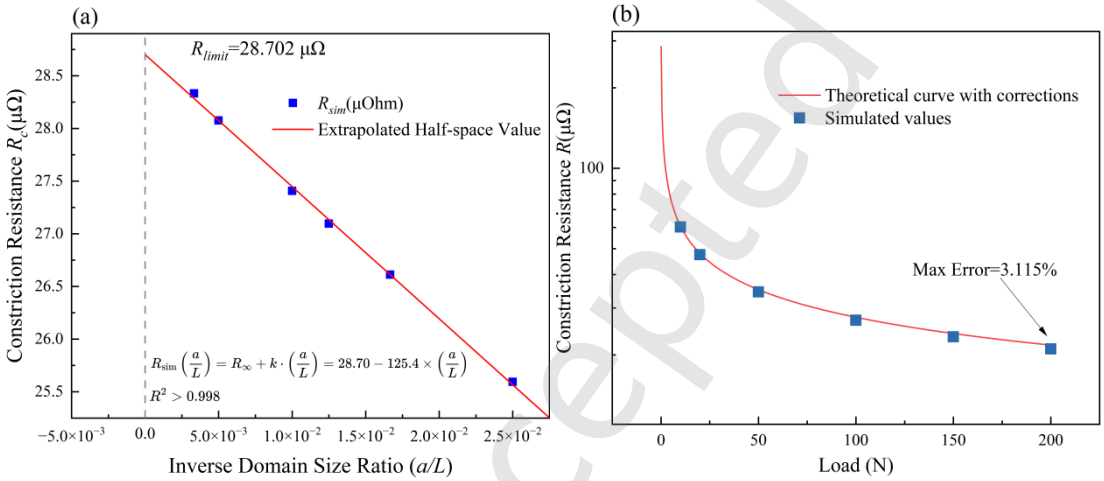


Fig. 6. Verification of the DC constriction resistance for a single circular contact spot: (a) variation of the constriction resistance R with a/L, together with the half-space limit obtained by linear extrapolation; (b) comparison between the numerical results for the constriction resistance as a function of load and the Holm theory.

In Eq. (11), when the frequency is zero, the formulation corresponds to the DC current case. We keep the contact spot radius a constant and gradually increase the computational domain size L. The ratio (a/L) is used to characterize the strength of the finite-domain effect. As shown in Fig. 6(a), the resulting constriction resistance R_{sim} has an approximately linear relation with a/L ($R^2 > 0.998$), which agrees well with the analytical solution of Holm. We further consider the effect of load, and the variation of contact resistance with load is shown in Fig. 6(b). Over the entire load range,

Just Accepted

the maximum relative error between the predictions of the proposed model and those of the Holm model remains below 3.115%. This error mainly comes from the geometric approximation of the periodic boundary of the finite domain and the circular contact boundary on a square grid. These results show that, in the DC limit, the conductive formulation correctly recovers the constriction-resistance behavior of an ideal single circular contact spot.

3.2 Finite-element verification of the variational capacitance bounds

The capacitance bounds in Section 2.3 are derived from variational principles. They are not obtained by fitting to numerical data. To verify their relation to the full electrostatic solution, we performed three-dimensional finite-element calculations for several representative gap geometries.

In all cases, the dielectric region between the two conducting surfaces was solved by the electrostatic equation $\nabla\cdot(\varepsilon\nabla\phi)=0$. The lower electrode was grounded, and the upper electrode was prescribed as $\phi = V_0$.

The lateral boundaries were electrically insulated. The finite-element capacitance was obtained from the total normal electric displacement on the upper electrode,

$$C_{\mathrm{FEM}} = \frac{1}{V_0}\left|\int_{\Gamma_{\mathrm{top}}} \mathbf{D}\cdot\mathbf{n}\,\mathrm{d}S\right|, \qquad \mathbf{D} = -\varepsilon\nabla\phi, \tag{38}$$

the analytical lower and upper estimates were evaluated on the projected domain Ω, consistent with the variational expressions in Section 2.3 and Appendix C.

The reference geometry was a parallel-plate capacitor with $L_x = L_y = 10\mu\mathrm{m}$, $g_0 = 1\mu\mathrm{m}$, $V_0 = 1\mathrm{V}$, $\varepsilon = \varepsilon_0$. The corresponding reference capacitance was

Just Accepted

$$C_0 = \frac{\varepsilon_0 L_x L_y}{g_0}. \tag{39}$$

For the parallel-plate case, the finite-element result coincides with C_0. This confirms the electrostatic boundary conditions, the charge integration, and the unit normalization. Three non-planar gap geometries were then considered.

First, a single sinusoidal upper surface was used,

$$h_1(x,y) = 0, \qquad h_2(x,y) = g_0 + a\cos\left(\frac{2\pi x}{L_x}\right), \tag{40}$$

the amplitude ratio a/g_0 was varied. As shown in Fig. 7(b), the finite-element capacitance increases with a/g_0, and it remains between the lower and upper bounds over the entire range. This confirms that the bounds correctly capture the effect of gap-height variation.

Second, the amplitude was fixed and the wavelength was varied,

$$h_2(x,y) = g_0 + a\cos\left(2\pi n\frac{x}{L_x}\right), \tag{41}$$

this changes the root-mean-square slope while keeping the gap-height distribution nearly unchanged for integer *n*. As shown in Fig. 7(c), the lower bound changes only weakly, whereas the upper bound increases with the surface slope. The finite-element solution remains between the two estimates. This result verifies that the difference between the two bounds is mainly associated with lateral electric-field energy induced by surface slopes.

Just Accepted

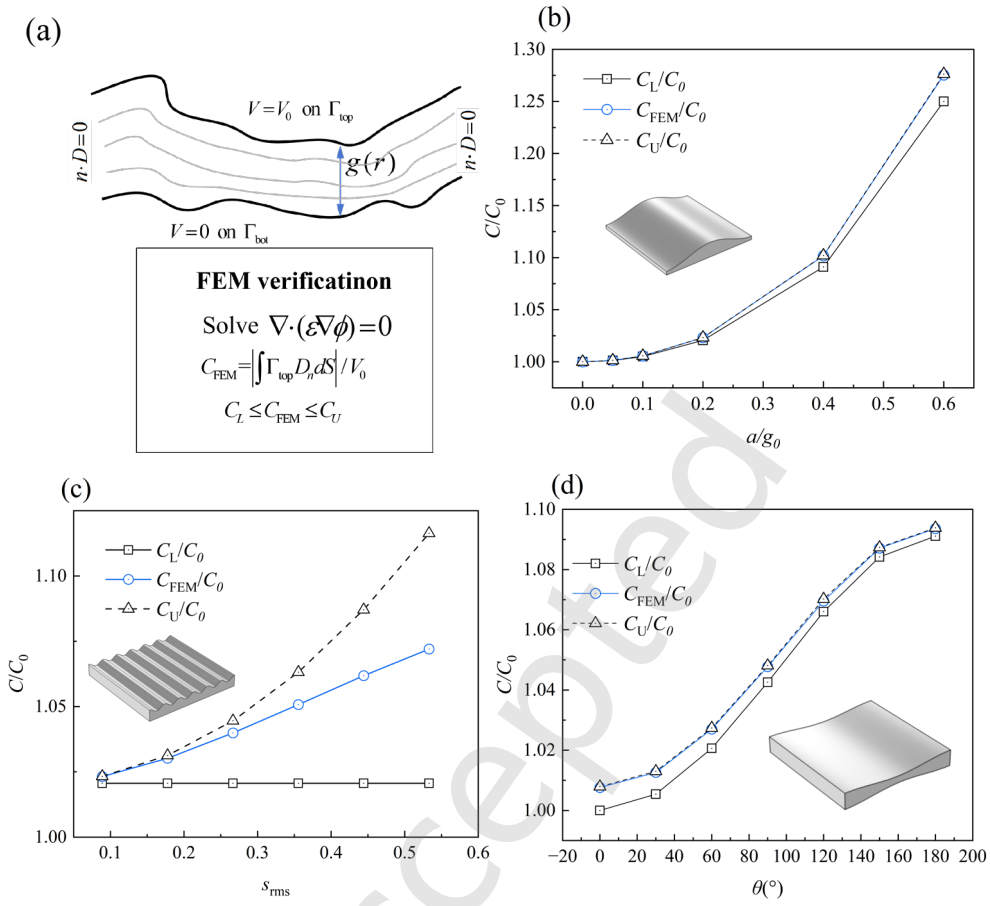


Fig. 7. Finite-element validation of the variational capacitance bounds for rough gaps: (a) schematic of the electrostatic problem and boundary conditions; (b) capacitance variation for a single sinusoidal surface with increasing amplitude a/g_0; (c) capacitance variation with RMS slope for a single sinusoidal surface with fixed amplitude and varying wavelength; (d) capacitance variation for two sinusoidal electrodes with different phase shifts θ. All capacitances are normalized by $C_0=\varepsilon_0 L_x L_y/g_0$.

Third, two sinusoidal electrodes with a phase difference were considered,

$$h_1(x,y)=z_{\text{off}}+b\cos(kx), \tag{42}$$

$$h_2(x,y)=z_{\text{off}}+g_0+b\cos(kx+\theta), \qquad k=\frac{2\pi}{L_x}, \tag{43}$$

the phase difference θ was varied from 0° to 180°. This case tests the two-surface slope-correlation term in the upper estimate. As shown in Fig. 7(d), the finite-element

Just Accepted

capacitance is again bounded by C_L and C_U.

When the two surfaces are in phase, the gap height is nearly uniform, but the electrodes are still curved. Therefore, C_{FEM} is slightly larger than C_L, which reflects the contribution from lateral electric-field components.

Overall, these finite-element results show that the variational estimates provide valid lower and upper bounds for the full three-dimensional electrostatic capacitance. They also clarify the physical meaning of the two estimates. The lower bound mainly reflects the local gap-height distribution, whereas the gap between the upper and lower estimates reflects the additional electrostatic energy associated with surface slopes and two-surface geometric correlation.

3.3 Verification against Bowler's analytical solution

Bowler derived an analytical solution for the electric field in a conducting half-space subjected to alternating current injection at the surface [34]. The solution follows directly from Maxwell's equations and is expressed using a transverse magnetic potential. For two surface contacts carrying equal and opposite currents, the total electric field is obtained by superposition. This solution provides an independent benchmark for the spectral surface impedance formulation in Section 2.2.

Bowler used the time dependence $e^{-i\omega t}$. After conversion to the $e^{i\omega t}$ convention adopted in the present work, the tangential electric field at the surface due to a point current I can be written as

$$E_{\rho}^{\mathrm{B}}(\rho,0)=\frac{I}{2\pi\sigma\rho^{2}}\left[e^{-\kappa\rho}+\kappa\rho\right],\qquad \kappa^{2}=i\omega\mu\sigma,\qquad \mathrm{Re}(\kappa)>0, \tag{44}$$

where ρ is the surface distance from the current injection point. For a source and

Just Accepted

return pair, the total surface field is obtained by linear superposition of the fields generated by the two contacts, as in Bowler's solution.

The configuration used in the present verification is shown in Fig. 8(a). The two outer contacts inject and extract currents $+\mathrm{I}$ and $-\mathrm{I}$, respectively. Their centers are located at $x = \pm s$. The two voltage probes are located at $x = \pm c$. The transfer impedance is defined as

$$Z_{4p} = \frac{\Delta U}{I}, \qquad \Delta U = V(-c) - V(c) = \int_{-c}^{c} E_x(x, 0)\, dx. \tag{45}$$

In the present calculation, $s = 2.5$ mm, $c = 1.25$ mm, and the current contact radius is $a = 0.5$ mm. Bowler's closed form above corresponds to a point current source. For the finite circular current contacts used here, the analytical reference is obtained by integrating Bowler's point source field over the same contact regions used in the spectral calculation. The conductor uses the conductivity and permeability listed in Table 1. The complex conductivity is reduced to σ in this benchmark to match the material model used by Bowler.

The injected and extracted currents have equal magnitudes and opposite signs. Therefore, the total normal current is zero and $\hat{j}_n(\mathbf{0}) = 0.$. Thus, the $q = 0$ mode does not enter this benchmark.

Figures 8(b) and 8(c) compare the magnitude and phase of Z_{4p} from 1 Hz to 100 MHz. The present model agrees closely with Bowler's analytical reference over the entire frequency range. The maximum relative difference in $|Z_{4p}|$ is approximately 0.081%, and the maximum phase difference is approximately 0.012°. The agreement is maintained from the low frequency limit to the frequency range in which

Just Accepted

electromagnetic diffusion becomes important.

These results verify the TM surface kernel and its spectral implementation for the nonzero Fourier modes. They also show that the closed source and return configuration is represented without any additional treatment of the $q = 0$ mode.

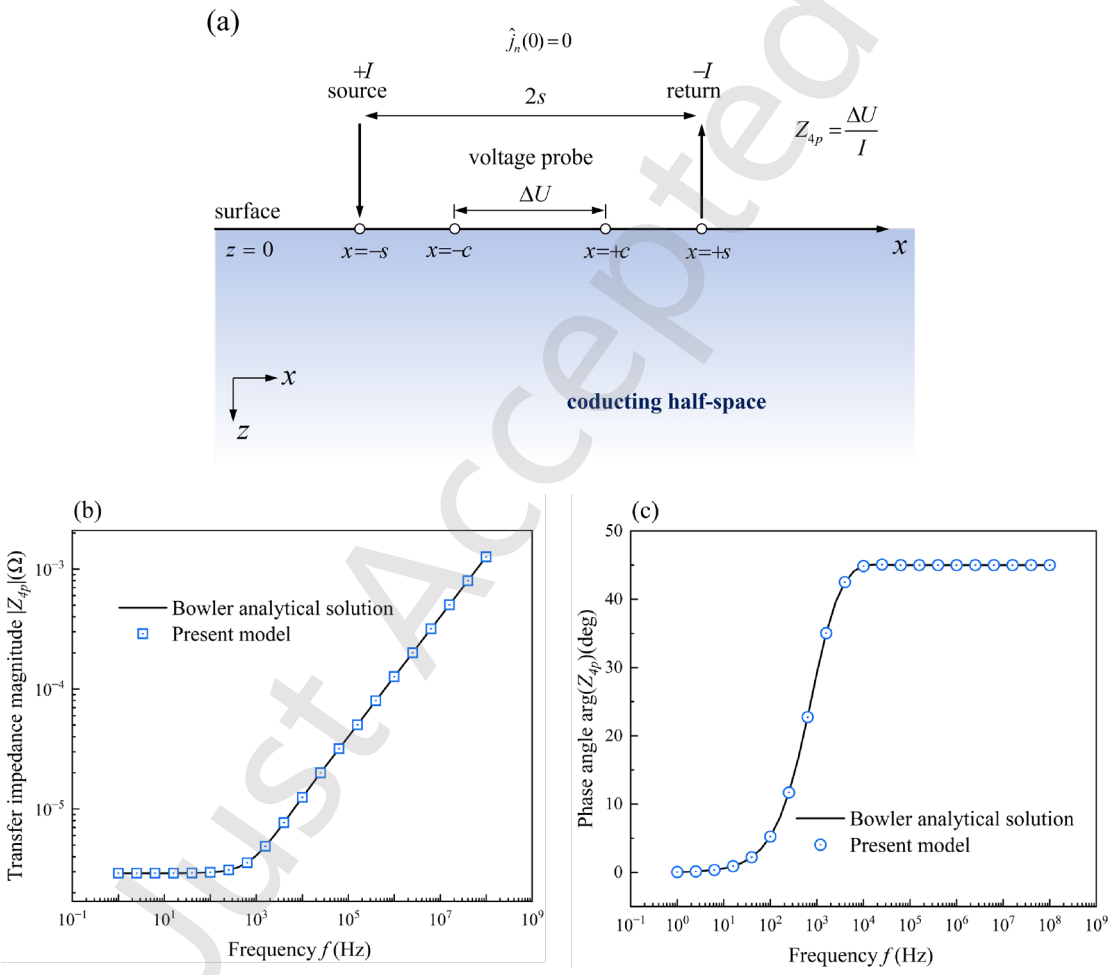


Fig. 8. Verification of the spectral surface impedance formulation against Bowler's analytical solution. (a) Conducting half-space with two current contacts at $x = \pm s$ and two voltage probes at $x = \pm c$. The outer contacts carry equal and opposite currents $+\mathrm{I}$ and $-\mathrm{I}$. (b) Magnitude of the transfer impedance Z_{4p}. (c) Phase angle of the transfer impedance Z_{4p}. The solid lines denote the analytical reference obtained from Bowler's solution, and the symbols denote the present model.

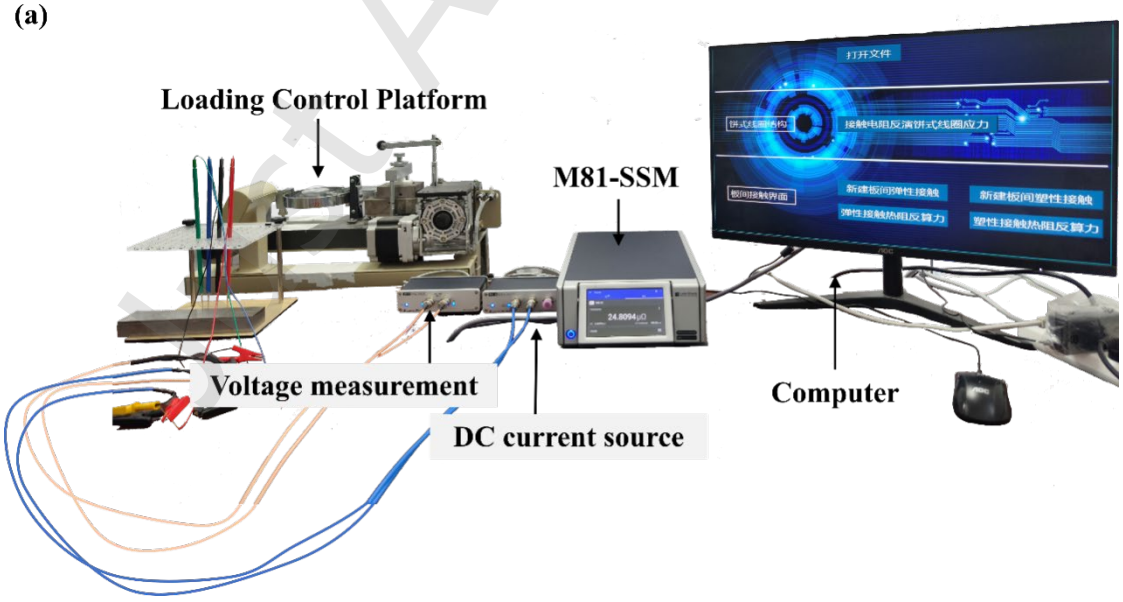
Just Accepted

3.4 Comparison with the response of rough interfaces under DC and AC conditions

We further assess the capability of the proposed method to predict the interfacial electrical response of random rough surfaces under multi-asperity contact conditions.

For the DC case, we conducted contact resistance measurements and compared the results with the volumetric contact model previously proposed by our group [35,36]. Copper was selected as the test material and machined by wire cutting into block specimens of different sizes. Contact surfaces with different roughness levels were then prepared through cleaning, polishing, sandblasting, and removal of the surface oxide layer with a brightening cleaner. Current-carrying tests were performed over a wide compressive load range from 1 N to 1000 N, and the source current was set to 10 mA to reduce the thermal effect caused by the current. The experimental setup is shown in Fig. 9. The experimental and numerical results are also shown in Fig. 10.

(a)



Just Accepted

(b)

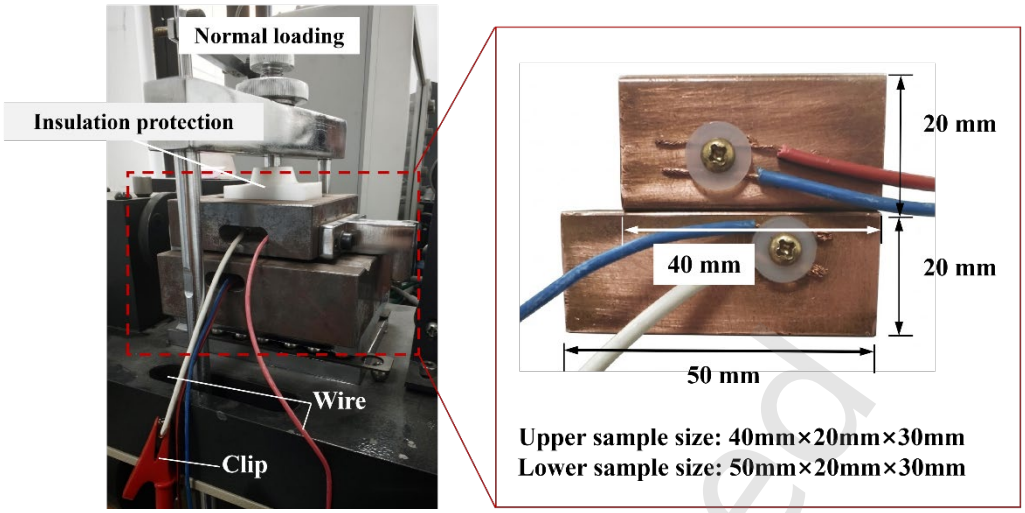


Fig. 9. Experimental setup for the DC electrical contact resistance test: (a) overall view of the test system; (b) photograph of the loading device and the test specimen.

As shown in Fig. 10, the present calculation reproduces the overall decrease in DC contact resistance with increasing load and remains close to the elastic branch of the volumetric contact model [35,36]. The remaining differences in absolute resistance, particularly at higher loads, should not be attributed to plastic deformation alone. Plasticity is one possible contributor, but specimen-specific roughness spectra and machining anisotropy, residual interfacial films, uncertainty in material parameters, and the idealized frictionless and adhesionless assumptions may also affect the comparison. The scope of the elastic assumption is discussed further in Section 5.

For the AC case, the numerical impedance results for rough interfaces reported by Wang et al. [12] are used as a reference. Their study considers the effects of surface roughness, normal load, oxide film thickness, and frequency on the interfacial impedance. However, the contact state is mainly obtained from the geometric truncation

Just Accepted

approximation in Ref. [37], and the actual elastic contact deformation and the associated detailed evolution of the gap field are not solved explicitly.

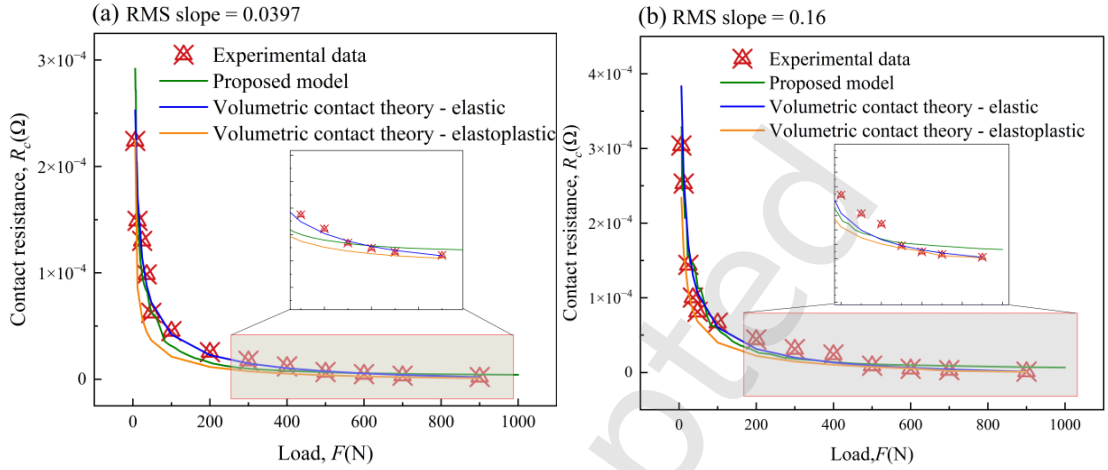


Fig. 10. Verification of DC contact resistance [35]: elastic modulus E = 117 GPa, Poisson's ratio v = 0.34, surface Hurst exponent H = 0.8, resistivity ρ = 1.75 ×10^{-8} Ω·m, yield strength σ_Y = 156 MPa. (a) q_0 = 4, q_1 = 4, q_2 = 128, RMS slope=0.0397; (b) q_0 = 4, q_1 = 20, q_2 = 128, RMS slope m_{rms} = 0.16.

The comparison in Fig. 11 shows that the proposed model and the model of Wang et al. predict the same trend of capacitance variation with load. However, the capacitance obtained from their geometric truncation method and finite element analysis is consistently higher than that predicted by the present model. This is because the geometric truncation method usually approximates the contact geometry as a rigidly truncated surface and neglects the actual local depression in the non-contact region induced by elastic deformation. As a result, it systematically underestimates the gap distance and overestimates the real contact area, which leads to an overprediction of capacitance. By contrast, the proposed model directly uses the actual contact state and

Just Accepted

gap field obtained from the mechanical solution as inputs. It therefore provides a more consistent description of the combined effect of conductive paths and capacitive bypasses in the non-contact region under AC conditions.

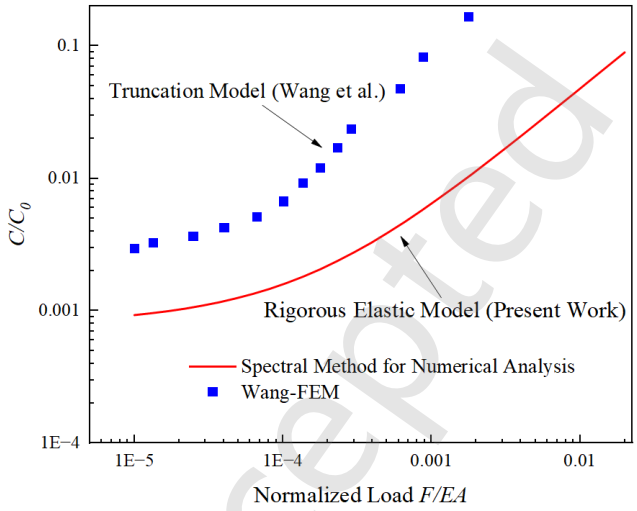


Fig. 11. Comparison of normalized interfacial capacitance as a function of normal load between the present model and the numerical results reported by Wang et al. (2021).

Just Accepted

4. Results

This section discusses how load, surface roughness, frequency, and the electrical boundary condition at the backside of the substrate affect the broadband impedance response of the contact interface. It also examines whether the resulting complex-impedance spectrum can serve as a load-dependent feature for normal-load identification.

4.1 Load and roughness dependence of broadband impedance

In this section, 30 independently generated rough-surface realizations are used to examine the evolution of the macroscopic complex impedance with the root-mean-

square slope and the nominal contact pressure $p_0 = F / A_0$. Unless otherwise stated, the numerical pressure range is $p_0 = 0.1 - 50$ MPa, corresponding to F = 10–5000 N for $A_0 = 100\ mm^2$. The dimensionless load used for normalization is stated together with p_0. To isolate the effect of interfacial microtopography from the nominal geometric size, the macroscopic electrical quantities are normalized by the nominal resistance and the nominal parallel-plate capacitance of a smooth, conforming interface. In Fig. 12, the solid lines and shaded bands denote the ensemble mean and one standard deviation, respectively.

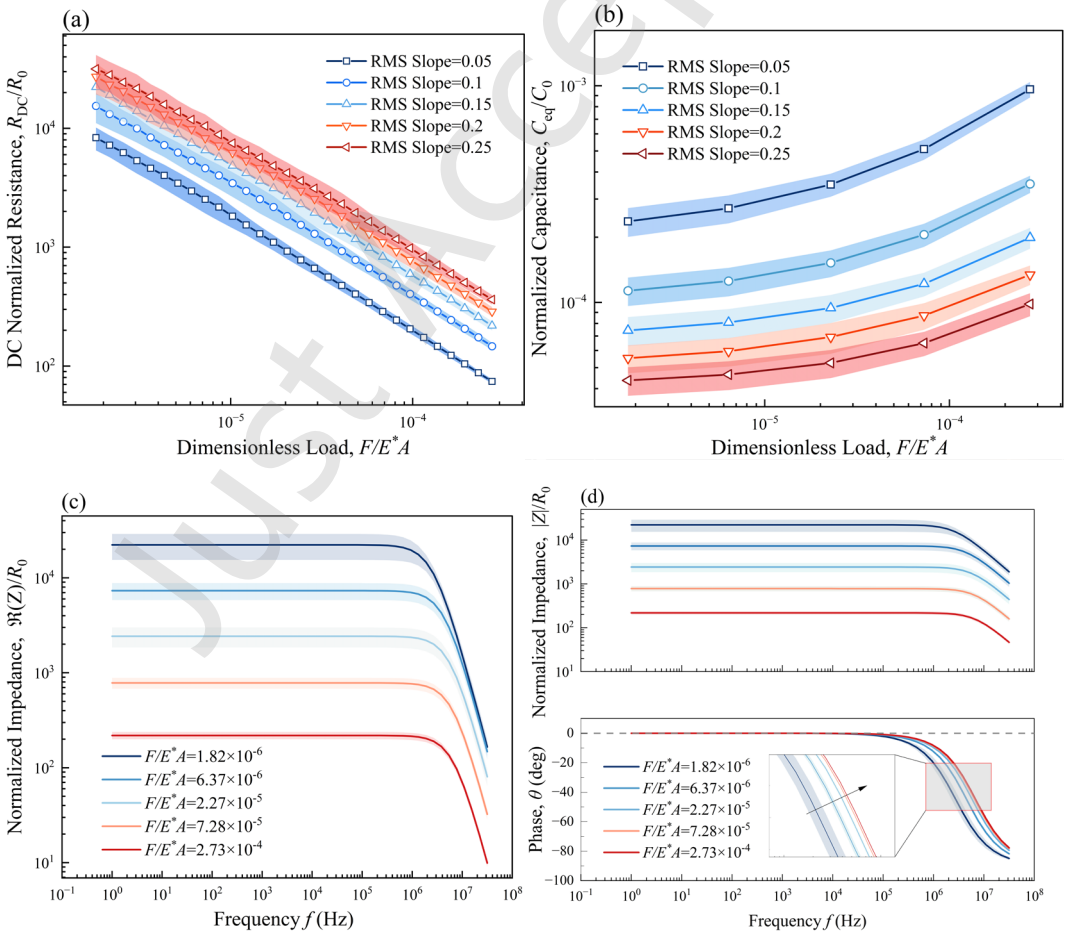


Fig. 12. Morphology-load coupling effects and broadband response characteristics of the contact impedance of rough interfaces: (a) scaling relation between normalized DC contact resistance and

Just Accepted

dimensionless load, for different surface roughness levels; (b) evolution of normalized equivalent interfacial capacitance with dimensionless normal load, for different surface roughness levels; (c) broadband dispersion characteristics of the real part of normalized AC contact impedance, for different dimensionless loads; (d) evolution of the magnitude and phase of the normalized complex contact impedance.

Fig. 12(a) shows that the normalized DC contact resistance R_{DC}/R_0 exhibits a power-law decay with the dimensionless load F/EA. As the load increases, surface asperities deform and the real contact area expands. The increase in effective conductive paths significantly weakens the current constriction effect. Meanwhile, surfaces with higher roughness show higher contact resistance over the entire load range because their contact spots are more discrete and sparser. Under AC excitation, the non-contact regions covered by the film layer form an equivalent gap capacitance of the interface. As shown in Fig. 12(b), with increasing load, the average interfacial gap is progressively compressed and the electrostatic coupling becomes stronger, which causes the normalized interfacial capacitance C_{eq}/C_0 to increase monotonically in a nonlinear manner. In contrast, a rougher surface provides stronger mechanical support from the asperity summits, which hinders further interfacial closure and thus keeps the equivalent capacitance at a lower level.

Fig. 12(c) and 12(d) reveal the dispersion behavior of the complex impedance of the contact interface under broadband excitation. In the low-frequency range, the system is dominated by conduction current through the real contact spots of asperities

Just Accepted

and therefore exhibits a purely resistive response, with the phase angle θ remaining at 0°, and $|Z|/R_0 \approx R_{DC}/R_0$. However, as the frequency increases and exceeds the critical cutoff frequency, the capacitive bypass through the film-covered region becomes active. The high-frequency AC signal then crosses the microscopic gaps in the non-contact region in the form of displacement current. As a result, both the real part of the impedance, $\Re\{Z\}/R_0$, and the total magnitude, $|Z|/R_0$, decrease, and the system undergoes a transition toward a capacitance-dominated state, with the phase angle θ approaching -90°. In addition, under a larger load, the contact resistance decreases markedly, which reduces the RC time constant of the system and shifts this transition to a higher frequency.

The shaded bands in Fig. 12 represent the standard deviations over 30 rough-surface samples. The larger scatter at low load arises from sparse asperity contacts, whereas increasing load activates more contact spots and makes the macroscopic response statistically more stable.

To further reveal the geometric origin of the load effect and the statistical dispersion shown in Fig. 12, Fig. 13 presents the contact state, the effective gap, and the distribution of local capacitive weights in the non-contact region for the same surface under low and high loads. As the load increases, both the real contact area fraction and the number of contact spots increase, while the corresponding normalized contact resistance decreases. At the same time, near-contact regions and narrow-gap regions increase markedly, which raises the normalized equivalent capacitance. This indicates that load reduces constriction resistance by enlarging the real contact region and, at the

Just Accepted

same time, enhances capacitive shunting by compressing the non-contact gaps; these two effects jointly determine the load dependence of the interfacial AC impedance.

The capacitive contribution is mainly concentrated in narrow gaps around contact spots. It appears as isolated hot spots at low load and develops into a broader network-like distribution at high load. This spatial evolution explains the reduced statistical scatter with increasing load.

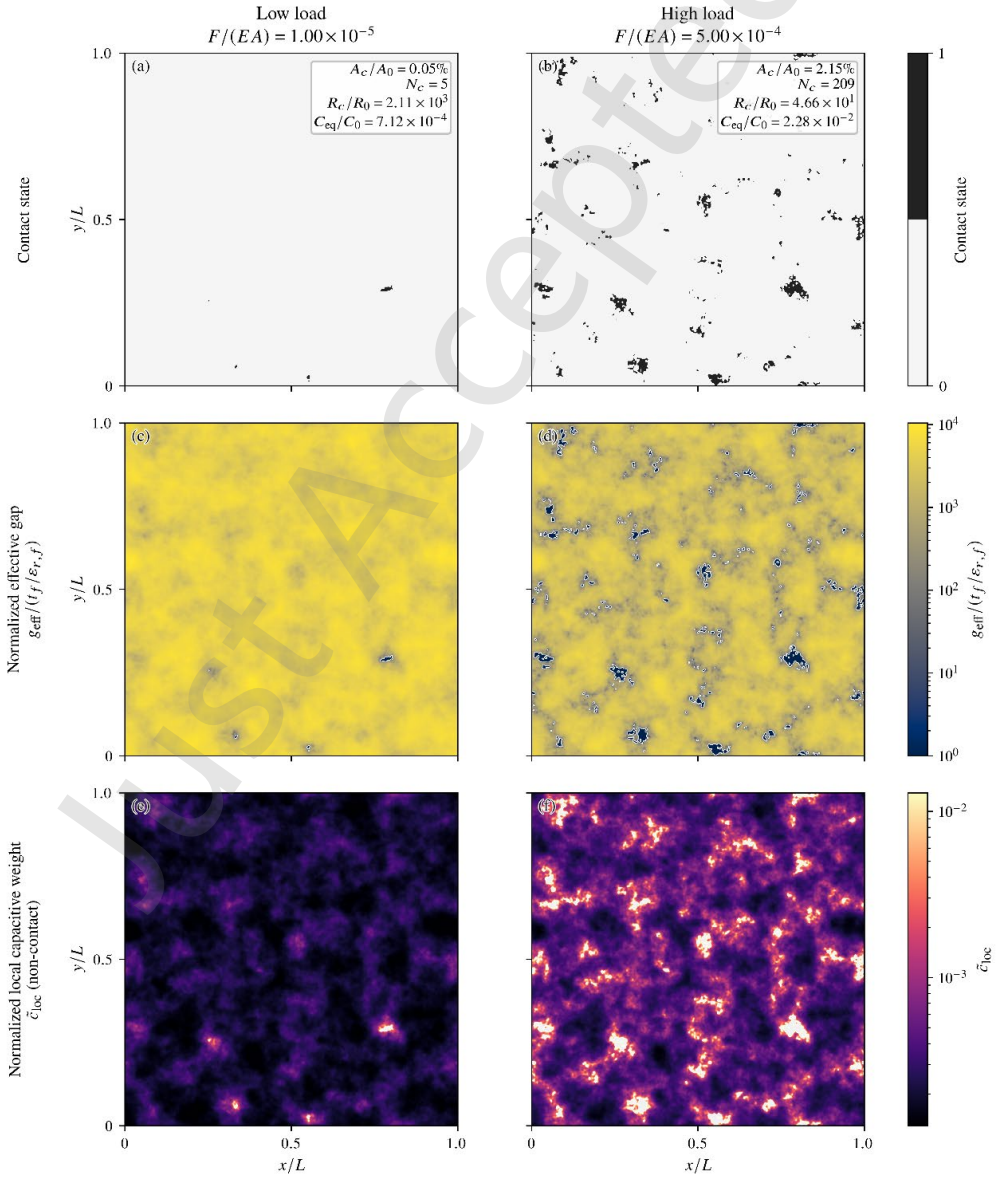


Fig. 13. Typical contact states of a rough interface, together with the effective gap and local capacitance distribution in the non-contact region, under low and high loads: (a, b) contact states

Just Accepted

under low and high loads; (c, d) corresponding distributions of the normalized effective gap $g_{eff}/\left(t_f/\varepsilon_{r,f}\right)$; (e, f) distributions of the normalized local capacitive weight $\%_{loc}$ in the non-contact region. The figure also shows the contact area fraction A_c/A_0, the number of contact spots N_c, the normalized contact resistance R_c/R_0, and the normalized equivalent capacitance C_{eq}/C_0. Here, $\%_{loc}=c_{\mathrm{loc}}/C_0$ denotes the local distribution associated with the integrand in Eq. (30), and integration over this quantity gives the global C_{eq}/C_0.

To quantify the characteristic size of the loaded contact regions without assigning a unique asperity radius to the self-affine surface, contact cells were grouped using periodic eight-neighbor connectivity. For each connected contact patch with area A_{patch}, an equivalent radius was defined as $a_{eq}=\sqrt{\frac{A_{patch}}{\pi}}$.. At $p_0=50$ MPa, the arithmetic mean of a_{eq} is 40.4 – 42.7 μm, and the largest equivalent radius is approximately 173.5 – 263.3 μm across the roughness levels considered. These values characterize the post-deformation contact patches at the present grid resolution and should not be interpreted as intrinsic, scale-independent asperity radii.

4.2 Finite thickness and backside boundary effects on the nonuniform conductive response

This section examines how conductor thickness and the backside electrical boundary affect the nonuniform conductive response of a rough contact. The surface, normal load, and mechanical contact state are fixed throughout the analysis. The representative contact has $m_{\mathrm{rms}}=0.10$, $F/(EA)=5\times10^{-4}$, and a nominal size of $L=10$ mm. The interfacial film and the displacement current across noncontact gaps

Just Accepted

are excluded. Therefore, all differences reported below arise from current propagation within the conductor and from the backside boundary.

The normal conductive current density is separated into its spatial mean, I / A, and a nonuniform component:

$$\Delta j(\mathbf{r}) = j(\mathbf{r}) - \frac{I}{A}, \qquad \int_A \Delta j(\mathbf{r}) \mathrm{d}A = 0. \tag{46}$$

For each backside condition b, the contact problem for the nonzero in-plane modes is written as

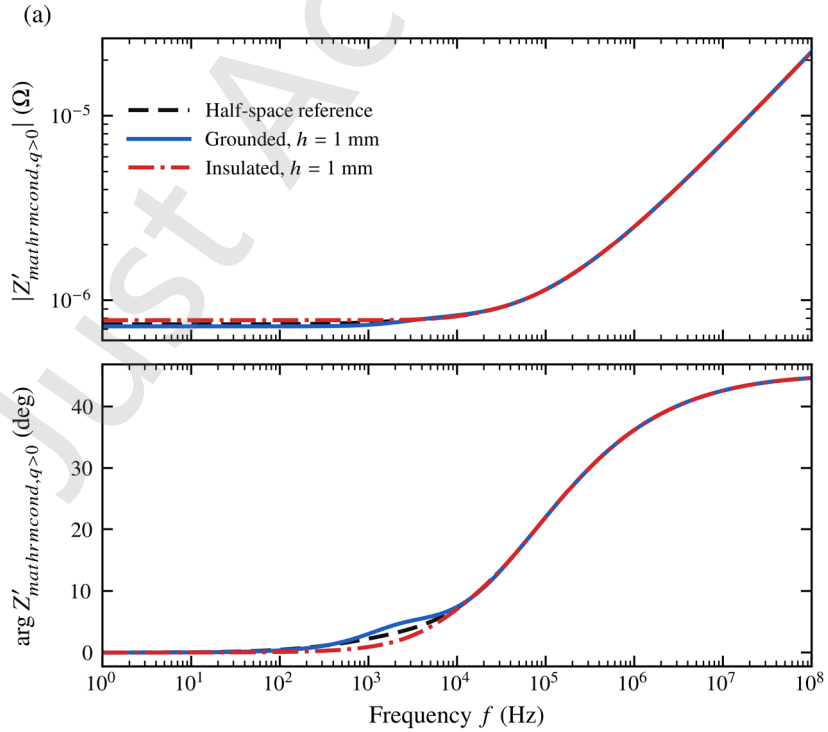
$$P_c K_b^{q>0} \Delta j = V_b' \mathbf{1}, \qquad Z_b' = \frac{V_b'}{I}. \tag{47}$$

here, P_c restricts the potential to the real contact region, $K_b^{q>0}$ is the surface kernel defined in Section 2.2, and V_b' is the common perturbation potential over that region. The quantity Z_b' describes the conductive impedance associated with the nonuniform current generated by rough contact. It does not include the spatially uniform $q = 0$ response, which depends on the external current path and terminal configuration. It is therefore not the complete terminal impedance.

Three ideal backside conditions are considered. The half-space case represents a conductor that is sufficiently thick for the relevant nonuniform modes to decay before reaching the backside. The grounded condition imposes $\phi(h) = 0$ at the backside. It approximates a large electrode with a low resistance connection that maintains an almost uniform potential. The insulated condition imposes $J_z(h) = 0$ and prevents normal current from crossing the backside. These conditions act on the same rough contact state and differ only in their constraint on current propagation inside the conductor.

Just Accepted

Fig. 14 compares the three responses for h = 1 mm over the frequency range from 1 Hz to 10^8 Hz. The absolute responses in Fig. 14(a) become almost identical at high frequency, but clear differences appear at low and intermediate frequencies. Fig. 14(b) shows these differences relative to the half-space response. For the grounded condition, the magnitude ratio reaches a minimum of about 0.968 and then shows a small maximum of about 1.006. Its largest positive phase difference is about 1.34°. For the insulated condition, the low-frequency magnitude ratio is about 1.053, while the largest negative phase difference is about -1.41°. The magnitude and phase differences can change sign in the transition range. Thus, neither finite thickness condition gives a uniform increase or decrease over the full frequency range. The response is determined by the complex propagation of the nonuniform current modes.



Just Accepted

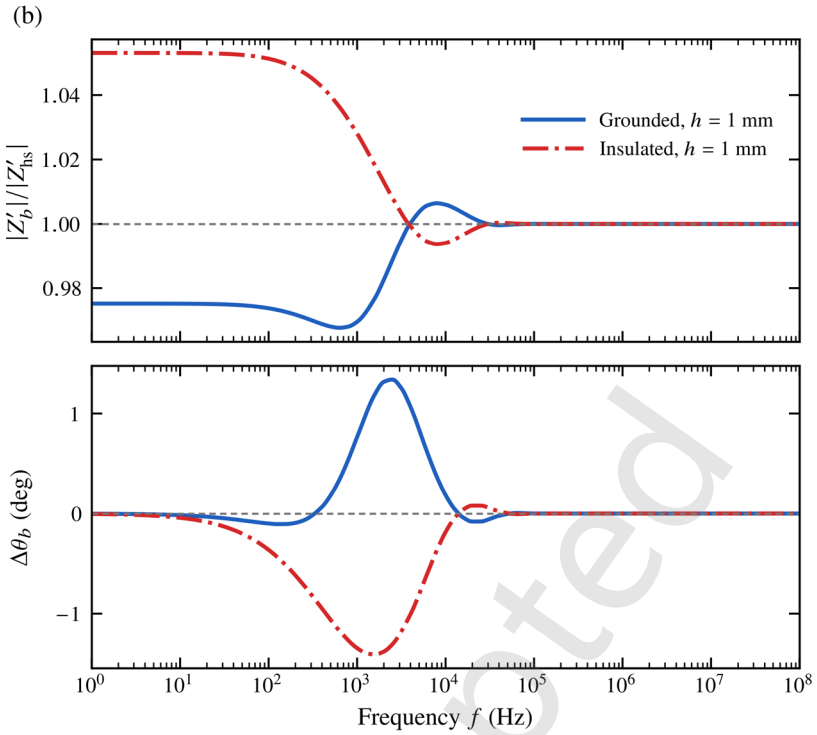


Fig. 14. Effect of the backside boundary on the nonuniform conductive response for a fixed rough contact and $h = 1$ mm. (a) Magnitude and phase of the q > 0 conductive impedance for the half-space, grounded, and insulated conditions. (b) Magnitude ratio $|Z'_b|/|Z'_{\mathbf{hs}}|$ and phase difference $\Delta\theta_b = \arg Z'_b - \arg Z'_{\mathbf{hs}}$ relative to the half-space response.

Fig. 15 shows the corresponding distribution of $|\mathbf{J}^{q>0}|$ inside the conductor. The frequency is $f = 1.585$ kHz, at which the insulated case for $h = 1$ mm has its largest absolute phase difference from the half-space response. The grounded condition fixes the backside potential but does not require the normal perturbation current to vanish there. In contrast, the insulated condition imposes $J_z^{q>0}(h) = 0$. These constraints produce different penetration and lateral redistribution of the current field. The bulk fields explain why the same mechanical contact state produces different surface responses under the two backside conditions.

Just Accepted

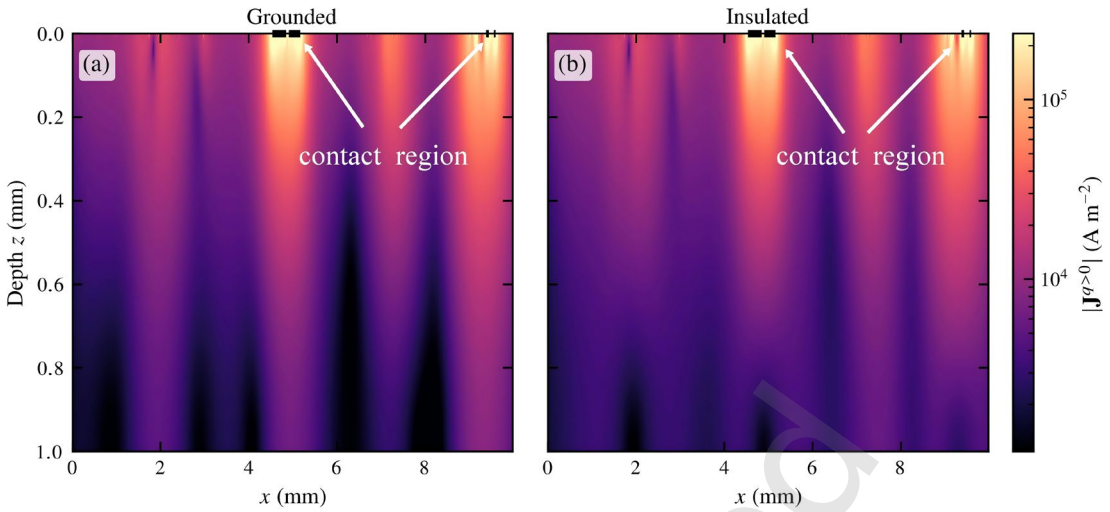


Fig. 15. Magnitude of the bulk current density associated with the nonzero in-plane modes for the same rough contact at $h = 1$ mm and $f = 1.585$ kHz: (a) grounded backside and (b) insulated backside. Both panels use the same color scale. The black segments at the top indicate the real contact regions along the selected section.

Fig. 16 shows how the backside sensitivity changes with conductor thickness. Five thicknesses from 0.1 to 10 mm are considered. The effect is strongest for the thinnest conductor. For $h = 0.1$ mm, the grounded magnitude ratio decreases to about 0.632 and later exceeds unity, while the insulated low-frequency ratio is about 2.02. The corresponding phase differences are also much larger than those for thicker conductors. As h increases, both the magnitude and phase deviations decrease. For $h = 10$ mm, the two finite thickness responses are already close to the half-space result over the full frequency range.

The thickness dependence is governed by the attenuation factor Γh, rather than by the ratio h/δ alone. For a good conductor,

Just Accepted

$$\Gamma^2 = q^2 + \mathrm{i}\omega\mu\sigma, \qquad (\Gamma h)^2 = (qh)^2 + 2\mathrm{i}\left(\frac{h}{\delta}\right)^2, \tag{48}$$

where q is the in-plane wavenumber and $\delta = \sqrt{2/(\omega\mu\sigma)}$ is the skin depth. The term qh describes attenuation associated with the lateral wavelength of each mode. The term h/δ describes attenuation caused by the skin effect. A mode becomes insensitive to the backside when either qh or h/δ is sufficiently large. Rough contact excites a broad range of q, so the total response is a weighted contribution from many modes. This explains why the curves do not collapse onto a single function of h/δ.

These results also clarify the relevance of the backside condition in experiments. A large electrode with a low-resistance connection may approach the grounded condition, whereas an insulating support may approach the insulated condition. The backside has the greatest influence when the conductor is thin and when long-wavelength current variations can penetrate through its thickness. At high frequency, the increase in $|\Gamma h|$ attenuates the nonuniform modes before they reach the backside, and all three responses approach the same limit. A complete model of a measured terminal impedance must additionally specify the $q = 0$ current path, terminal geometry, interfacial film, and gap displacement current.

Just Accepted

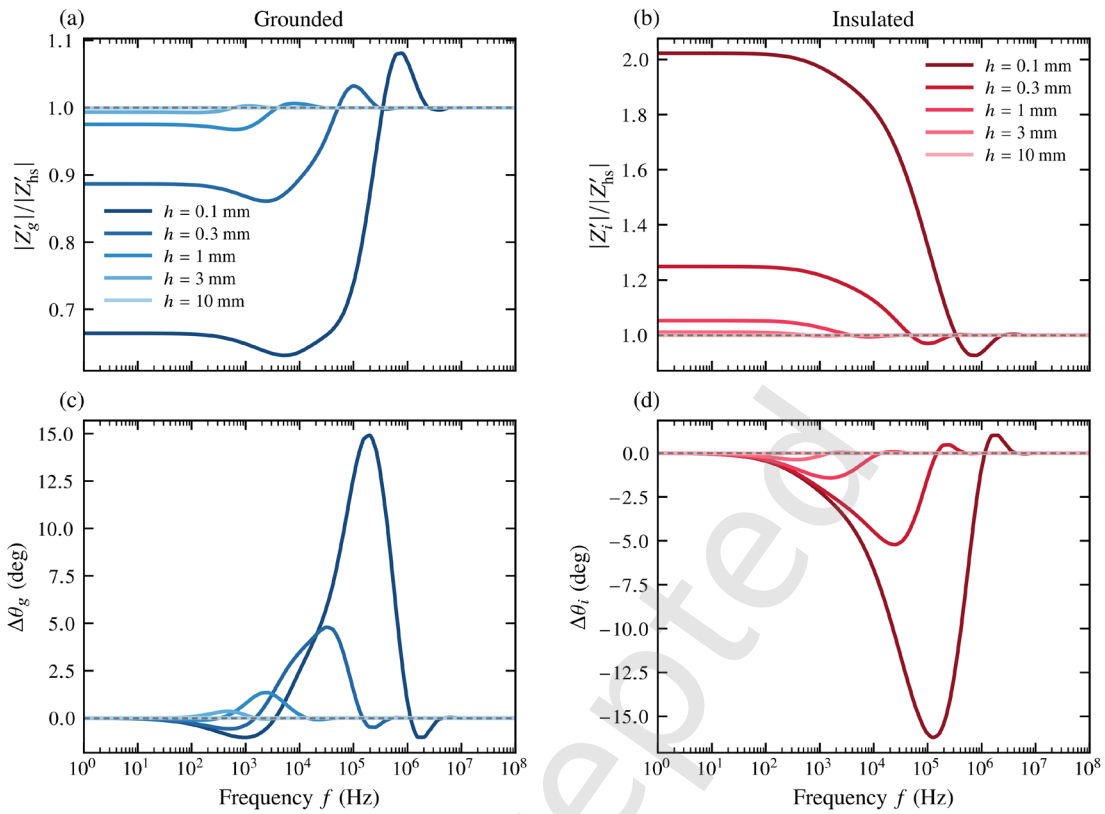


Fig. 16. Dependence of the backside sensitivity on conductor thickness and frequency for the same rough contact. (a) Grounded magnitude ratio $|Z'_g|/|Z'_{\mathbf{hs}}|$, (b) insulated magnitude ratio $|Z'_i|/|Z'_{\mathbf{hs}}|$, (c) grounded phase difference $\Delta\theta_g$, and (d) insulated phase difference $\Delta\theta_i$. The thicknesses are $h = 0.1$, 0.3, 1, 3, and 10 mm.

4.3 Load-frequency criterion for capacitive relevance

This section further discusses the conditions under which the displacement current paths in the non-contact region are generally not negligible. Under the modeling framework in Section 2, the total admittance of a rough interface consists of a conductive branch and a capacitive branch connected in parallel. Therefore, whether the air-gap capacitance can be neglected essentially depends on the relative competition between these two types of paths, rather than on the geometric gap alone. At the same

Just Accepted

time, the calculation of the non-contact capacitance must be regularized by introducing a minimum effective gap or an equivalent series thickness. Otherwise, when the local gap approaches zero, a purely geometric integral loses a meaningful upper bound.

Fig. 17(a, b) shows the variations of C_{gap} and the crossover frequency $f_c = 1/\left(2\pi R_c C_{\mathrm{gap}}\right)$ with load. As the normal load increases, the mean interfacial gap is progressively compressed, and the electrostatic coupling in the non-contact region becomes stronger. As a result, C_{gap} increases monotonically. At the same time, the expansion of the real contact area causes the contact resistance to decrease continuously, which shifts f_c markedly toward higher frequencies. This indicates that, within the present model and parameter range, the importance of the air-gap capacitance is not determined by C_{gap} alone. Instead, it is jointly governed by the decrease in R_c and the increase in C_{gap}. In other words, the higher the load, the more the system remains approximately resistive at higher frequencies. Under low-load conditions, the capacitive shunting path enters the observable range earlier.

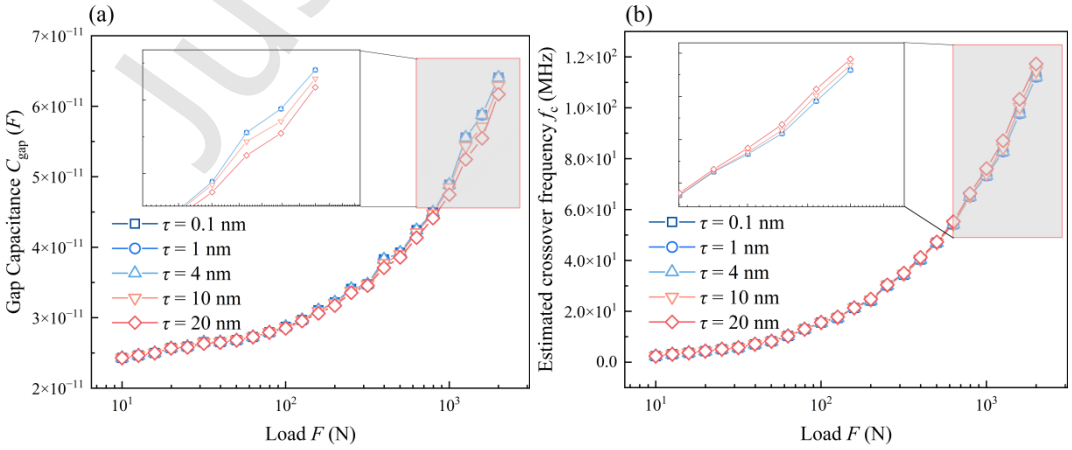


Fig. 17. (a) Variation of the gap capacitance C_{gap} with load for different truncation distances τ; (b) variation of the cutoff frequency f_c with load for different truncation distances.

Just Accepted

Fig. 17 also shows that the differences among the curves for different τ are not uniform. For $\tau = 0.1-4$ nm, the curves almost overlap. Discernible shifts in C_{gap} and f_c appear only when τ increases to 10–20 nm. This means that, under the present uniform film model, the upper bound of the capacitance is not controlled by τ alone. It is jointly determined by τ and the equivalent series thickness of the film. Fig. 18 shows this more clearly: when τ is smaller than t_f/ε_r, $C_{\text{gap}}(\tau)/C_{\text{gap}}(1\,\text{nm})$ stays essentially on a plateau. The capacitance starts to decrease appreciably only after τ approaches and exceeds t_f/ε_r, while the corresponding f_c increases accordingly. Therefore, for the uniform film model used in this work, the effective lower bound for capacitive closure is $G_{\min}^{\text{eff}} = \max\left(\tau, \frac{t_f}{\varepsilon_{r,f}}\right)$, rather than the nominal value of τ itself. Consequently, when $\tau < t_f/\varepsilon_{r,f}$, variations in τ do not change the actual lower bound of $G_{eff}(r)$.

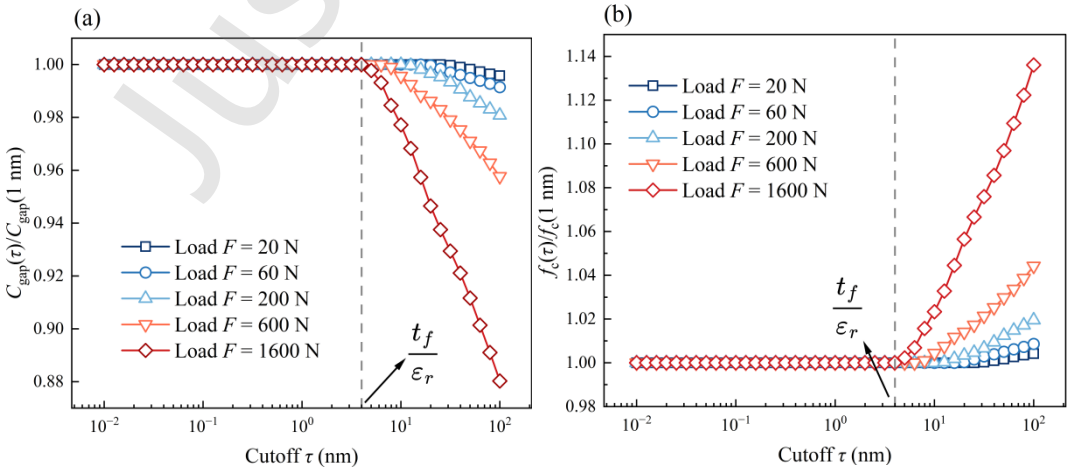


Fig. 18. (a) Under a representative load, variation of the normalized gap capacitance $C_{gap}(\tau)/C_{gap}(1\,\text{nm})$ with truncation distance τ; (b) under a representative load, variation of

Just Accepted

the normalized cutoff frequency $f_c(\tau)/f_c(1\ \mathrm{nm})$ with truncation distance τ.

Fig. 19 provides load-frequency maps for judging whether the gap capacitance should be included. The boundary curves for both criteria move to higher frequencies with increasing load, indicating that higher load delays the onset of capacitive relevance. The physical meaning of the selected thresholds can be understood from the ideal parallel RC limit. If $Y_{\mathrm{tot}} = 1/R_c + j\omega C_{\mathrm{gap}}$ and $\eta = \omega R_c C_{\mathrm{gap}} = f/f_c$, then $|\theta| = \arctan\eta$, while the relative magnitude deviation from the purely resistive approximation is $1 - |Z|/R_c = 1 - (1+\eta^2)^{-1/2}$. Thus, a 5° phase shift corresponds to $\eta = \tan 5^\circ \approx 0.087$, whereas a 5% magnitude deviation corresponds to $\eta \approx 0.329$. This explains why the phase threshold appears earlier than the magnitude-deviation threshold: the phase is first-order sensitive to the capacitive branch, whereas the magnitude deviation is second-order sensitive for small η. Therefore, the thresholds of 5° and 5% are used as illustrative engineering criteria rather than universal critical values.

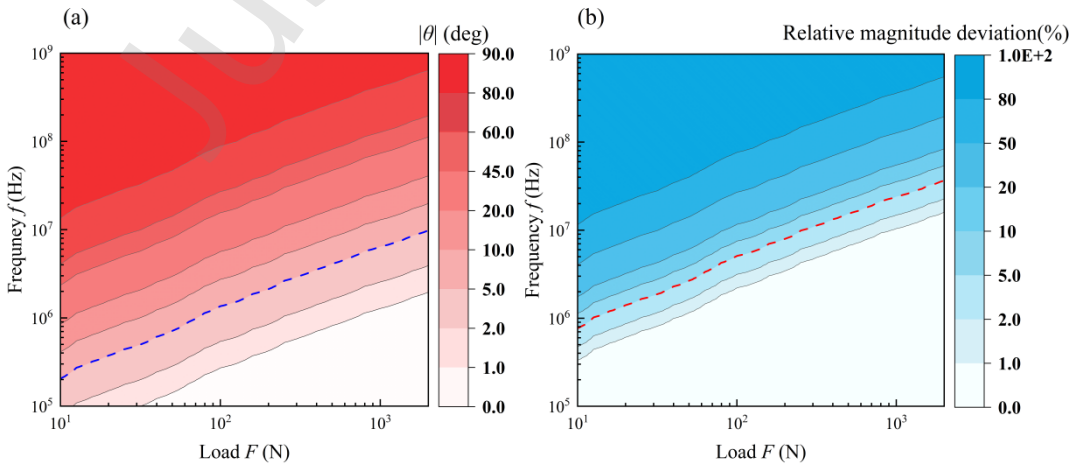


Fig. 19. (a) Load-frequency map of the phase magnitude $|\theta|$, with the 5° threshold boundary

Just Accepted

marked; (b) load-frequency map of the relative magnitude deviation, with the 5% threshold boundary marked.

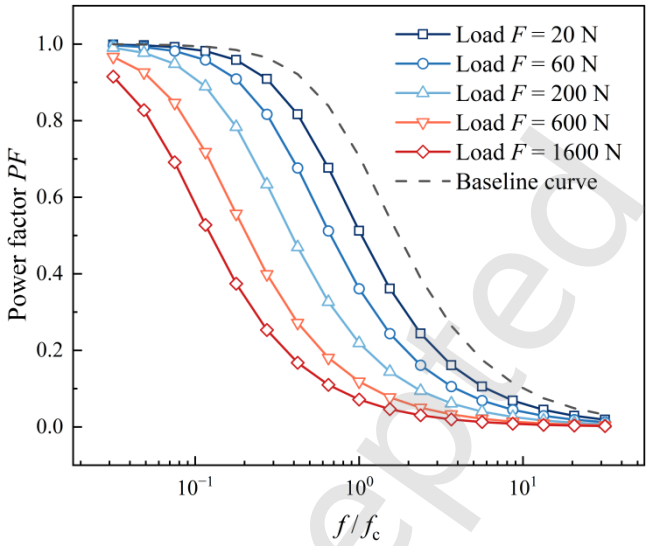


Fig. 20. Comparison of the power factor as a function of normalized frequency between the estimate from the simplified parallel RC model and the simulation results obtained in this study.

Finally, Fig. 20 compares the full broadband results with a simplified parallel RC estimate. If the interface can be strictly represented by an ideal lumped R || C network, the PF curves at different loads should collapse onto the same reference curve when plotted against f / f_c. The power factor is defined here as $PF = \cos|\theta|$, where θ is the impedance phase angle. However, the results show that the calculated curves shift overall toward lower f / f_c, and this shift becomes more pronounced as the load increases. This observation indicates that, although f_c provides a convenient and effective first-order estimate for quickly judging when the capacitive shunting path starts to become significant, it is not a strictly universal parameter. The reason is that

Just Accepted

the conductive branch in this work is not an ideal constant resistor. Instead, it is a dispersive branch jointly determined by the layered-medium transmission-line kernel and the contact mixed boundary-value problem. Therefore, the real system often enters the regime where capacitive effects cannot be neglected earlier than predicted by the parallel RC model.

4.4 Impedance-based load identification under amplitude gain-bias uncertainty

The previous sections show that the impedance of the rough contact interface depends on both load and frequency. This means that the impedance spectrum can also be viewed as a load-dependent signal feature. This interpretation is consistent with impedance- and admittance-based monitoring studies, where broadband impedance-related signatures have been used as informative features for damage detection and mechanical-state assessment [38,39]. To examine this point, we performed a synthetic inverse test. The purpose of this test is not to provide experimental validation. It is used to evaluate whether the simulated impedance signatures contain enough information to identify the normal load under measurement uncertainty.

For a given true load F_{true}, the model first gives the complex impedance spectrum $Z(f_i, F_{\text{true}})$. A synthetic observed impedance was then generated by adding a correlated amplitude gain bias to the magnitude channel, $\ln|Z(f_i, F_{\text{true}})| + b + \text{ò}_i$, , where b is a constant amplitude bias shared by all frequency points, and ò_i is a small independent random noise term. This bias represents possible amplitude calibration errors, cable or fixture gain drift, and other multiplicative errors in the measured impedance magnitude. The phase channel was perturbed independently as $\phi_{\text{obs}}(f_i) = \phi(f_i, F_{\text{true}}) + \eta_i$..

Just Accepted

Two representative inverse features were compared. The first one is a single low-frequency resistance-like feature. It estimates the load by matching only the lowest-frequency impedance magnitude, $\hat{F}_{\mathrm{LF}} = \arg\min_F \left[\ln|Z_{\mathrm{obs}}(f_0)| - \ln|Z(f_0,F)|\right]^2$.. The second one is the broadband complex-impedance feature. It uses the whole impedance spectrum. To account for the unknown amplitude bias, a constant log-amplitude offset is fitted for each candidate load, $b^*(F) = \frac{1}{N_f}\sum_i \left[\ln|Z_{\mathrm{obs}}(f_i)| - \ln|Z(f_i,F)|\right]$.. The load is then identified by minimizing the combined magnitude-shape and phase residual, $\hat{F}_{\mathrm{CI}} = \arg\min_F \frac{1}{N_f}\sum_i \left[\frac{\ln|Z(f_i,F)| + b^*(F) - \ln|Z_{\mathrm{obs}}(f_i)|}{\sigma_m}\right]^2 + \left[\frac{\phi(f_i,F) - \phi_{\mathrm{obs}}(f_i)}{\sigma_\phi}\right]^2$..

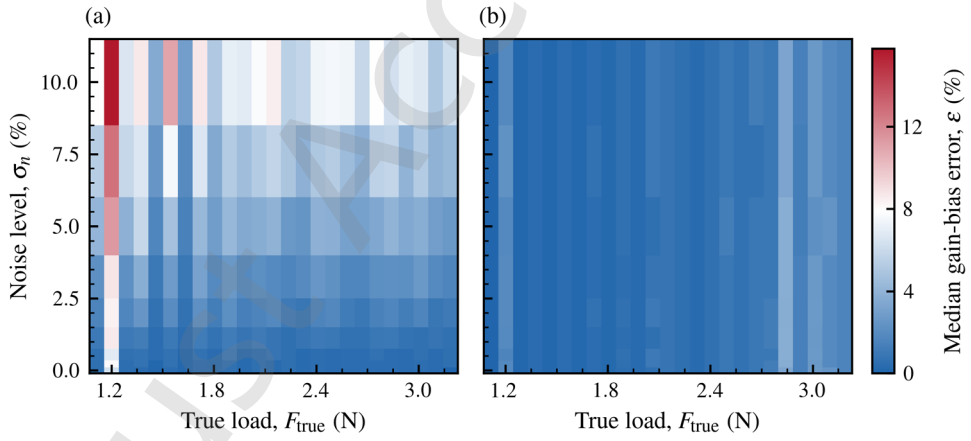


Fig. 21. Synthetic load-identification test under correlated amplitude gain-bias uncertainty. The horizontal axis is the logarithmic true load, $\log_{10}(F_{\mathrm{true}}/1\mathrm{N})$, and the vertical axis is the amplitude gain-bias level, σ_b. The color denotes the median absolute load-identification error e_F. Panel (a) uses a single low-frequency resistance-like feature. Panel (b) uses the broadband complex-impedance spectrum with a fitted amplitude bias and phase information.

Just Accepted

The identification error is defined as $e_F = \left| \frac{\hat{F} - F_{\text{true}}}{F_{\text{true}}} \right| \times 100\%$.. Fig. 21 shows the load-identification error over the load–bias domain. The single low-frequency feature becomes more sensitive to amplitude gain bias as the bias level increases. The error also shows stronger local variation with load. In contrast, the broadband complex-impedance feature keeps a lower error over most of the domain. This result indicates that the broadband impedance spectrum provides a more robust load signature than a single resistance-like feature. The improvement comes from two sources. First, the spectrum contains multi-frequency information, so the load is constrained by the shape of the response rather than by one scalar value. Second, the phase response provides an additional constraint that is not directly affected by amplitude gain bias.

This inverse test remains model-based. It does not replace direct broadband impedance measurements. It only shows that, within the proposed model, the complex impedance spectrum contains useful information for load identification under controlled measurement uncertainty.

5. Discussion

The calculations show that load influences the AC response through two geometric channels. Enlargement of the real contact region reduces constriction resistance, whereas compression of the non-contact gaps increases capacitive shunting. Frequency determines the relative importance of these two branches. The finite-thickness and backside electrical conditions further modify the nonuniform conductive response when the relevant current modes penetrate to the backside of the conductor.

For the linear-elastic half-space model, the interfacial deformation scales with

Just Accepted

p_0 / E^* for a fixed dimensionless topography and Poisson's ratio. Thus, at a given nominal pressure, a lower effective modulus generally produces larger deformation, a larger real contact area, and smaller residual gaps, which tend to decrease the conductive resistance and increase the gap capacitance. Different PSD bandwidths, correlation lengths, and anisotropic machining textures will consequently change the detailed pressure–contact-state–impedance relation. In the present one-way coupling framework, the mechanical constitutive law does not enter the electrical operator directly. Its influence is transmitted through the deformed contact-state field $m(\mathbf{r})$ and gap field $g_m(\mathbf{r})$. The electrical formulation can therefore be coupled to measured interface fields or to anisotropic and elastoplastic contact solvers without changing the subsequent electrical equations.

The numerical range $p_0 = 0.1 \sim 50$ MPa should not be interpreted as a universal elastic range. In a multiscale rough contact, yielding initiates locally within microcontacts and depends on the material yield properties, RMS slope, PSD bandwidth, and short-wavelength cutoff [40,41]. For a specified ductile material and resolved surface, a more meaningful local screening parameter can be defined as $\chi_y = \dfrac{\max_{\mathbf{r},z} \sigma_{eq}^{el}(\mathbf{r},z)}{\sigma_y}$,, where σ_{eq}^{el} is the von Mises equivalent stress predicted from the elastic solution and σ_y is the material yield strength. A value $\chi_y < 1$ indicates that no local yielding is predicted at the adopted surface resolution and within the assumed material model, whereas χ_y approaching or exceeding unity indicates that elastoplastic deformation should be considered. Once yielding occurs, the subsequent contact state also depends on the hardening law and loading history. Because specimen-

Just Accepted

specific elastoplastic parameters were not calibrated in the present work, the elastic contact solution is used as an idealized mechanical baseline rather than as a quantitative prediction for a particular metal over the full nominal-pressure range.

The present model does not include film rupture, wear, local Joule heating, dielectric breakdown, or two-way thermoelectromechanical coupling, and the dielectric film is represented by a spatially uniform equivalent layer. These effects may become important under severe loading or high-field conditions. In addition, the synthetic inverse test is model-based and does not replace direct broadband impedance measurements. It only demonstrates that, within the present framework, the spectral shape and phase provide load information that is less sensitive to correlated amplitude gain bias than a single low-frequency magnitude.

6. Conclusions

The principal conclusions are as follows.

(1) The Maxwell-based TM surface-impedance formulation recovers both the direct-current constriction limit and the finite-frequency half-space response. The maximum relative error with respect to Holm's a-spot solution is below 3.115%, while comparison with Bowler's analytical solution gives maximum differences of approximately 0.081% in impedance magnitude and 0.012° in phase.

(2) Over the numerical pressure range $p_0 = 0.1 \sim 50$ MPa, increasing load modifies both interfacial transport branches. Enlargement of the real contact regions reduces constriction resistance, whereas compression of the remaining gaps increases capacitance. Their combined evolution shifts the onset of capacitive relevance toward

Just Accepted

higher frequencies. Statistics over 30 independent rough-surface realizations show larger impedance scatter at low load, where transport is controlled by sparse contact spots, and reduced scatter as additional contact regions become active.

(3) For a fixed rough-contact state, conductor thickness and backside electrical constraints affect the nonuniform $q > 0$ conductive response. At h=1 mm, the grounded and insulated conditions produce maximum phase deviations of approximately $+1.34^{\circ}$ and -1.41°, respectively, relative to the half-space response. At h=0.1 mm, the grounded magnitude ratio decreases to approximately 0.632, whereas the insulated low-frequency magnitude ratio reaches approximately 2.02. These deviations diminish when the conductor becomes sufficiently thick or when the relevant modes are attenuated at high frequency.

(4) In the synthetic inverse test, the broadband magnitude–phase spectrum provides a more robust load-sensitive feature under correlated amplitude gain-bias uncertainty than a single low-frequency resistance-like quantity. This result supports broadband impedance as a candidate feature for contact-state monitoring, while direct experimental validation and material-calibrated elastoplastic and interfacial-film models remain necessary for quantitative applications.

Just Accepted

Appendix

Appendix A. Governing Equations Inside the Conductor and TM Spectral Reduction

This appendix gives the Maxwell-based derivation of the spectral surface relation used in Section 2.2. Consider a linear, isotropic, and homogeneous medium, and take

the time factor as $e^{j\omega t}$. The frequency-domain Maxwell equations are

$$\nabla \times \mathbf{E} = -j\omega \mathbf{B}, \quad \nabla \times \mathbf{H} = \mathbf{J} + j\omega \mathbf{D}, \quad \nabla \cdot \mathbf{D} = \rho_v, \quad \nabla \cdot \mathbf{B} = 0, \tag{A1}$$

the constitutive relations are

$$\mathbf{B} = \mu \mathbf{H}, \quad \mathbf{D} = \varepsilon \mathbf{E}, \quad \mathbf{J} = \sigma \mathbf{E}, \tag{A2}$$

and the complex conductivity is introduced as

$$\tilde{\sigma} = \sigma + j\omega\varepsilon. \tag{A3}$$

Ampère's law then becomes

$$\nabla \times \mathbf{H} = \tilde{\sigma}\mathbf{E}. \tag{A4}$$

For a homogeneous medium, the magnetic field satisfies

$$\nabla^2 \mathbf{H} - \gamma^2 \mathbf{H} = 0, \qquad \gamma^2 = j\omega\mu\tilde{\sigma}. \tag{A5}$$

We now consider a nonzero in-plane Fourier mode $\mathbf{q} = (q_x, q_y)$, with $q = |\mathbf{q}| > 0$. For each $q > 0$, the field can be decomposed into transverse-electric (TE) and transverse-magnetic (TM) components with respect to the $(\mathbf{q}, z)$ plane. Since the TE component has $E_z = 0$, it carries no normal current and therefore does not contribute to the surface mapping considered here; only the TM component is retained. Normal-current excitation couples to the TM mode, for which the magnetic field can be written as

$$\mathbf{H} = H_s(\mathbf{q}, z)\left(\mathbf{e}_z \times \hat{\mathbf{q}}\right). \tag{A6}$$

where $\hat{\mathbf{q}} = \dfrac{\mathbf{q}}{q}$. Ampère's law gives

$$\mathbf{E}_t = -\frac{1}{\tilde{\sigma}} \frac{\partial H_s}{\partial z} \hat{\mathbf{q}}, \qquad \hat{j}_n = \tilde{\sigma}\hat{E}_z = jqH_s. \tag{A7}$$

The spectral surface-potential variable is defined through the tangential electric

Just Accepted

field as

$$\mathbf{E}_t = -j\mathbf{q}\hat{\phi}. \tag{A8}$$

Combining these relations gives

$$\frac{d^2\hat{\phi}}{dz^2} - \Gamma^2\hat{\phi} = 0, \qquad \hat{j}_n = -\sigma\frac{q^2}{\Gamma^2}\frac{\partial\hat{\phi}}{\partial z}, \tag{A9}$$

where $\Gamma^2 = q^2 + j\omega\mu\sigma$

Thus, $\hat{\phi}$ is a Fourier-domain surface-potential variable defined by the tangential electric field. In the dc limit, $\Gamma \to q$, and the resulting surface kernel reduces to $1/(\sigma q)$, recovering the classical dc constriction formulation.

Appendix B. In-Plane Fourier Transform, Layered Surface Impedance Kernels, and Discrete Operators

B.1 In-Plane Fourier Representation and One-Dimensional Modal Equation

Let $\mathbf{r} = (x, y)$, $\mathbf{q} = (q_x, q_y)$, and $q = |\mathbf{q}|$. We use the following two-dimensional Fourier transform pair:

$$\begin{aligned} \hat{f}(\mathbf{q}, z) &= \iint_{R^2} f(\mathbf{r}, z) e^{-i\mathbf{q}\cdot\mathbf{r}}\, d^2r, \\ f(\mathbf{r}, z) &= \frac{1}{(2\pi)^2} \iint_{R^2} \hat{f}(\mathbf{q}, z) e^{j\mathbf{q}\cdot\mathbf{r}}\, d^2q \end{aligned} \tag{B1}$$

For the TM potential variable introduced in Appendix A, each nonzero in-plane Fourier mode $q > 0$ satisfies

$$\frac{d^2\hat{\phi}}{dz^2} - \Gamma^2\hat{\phi} = 0, \qquad \Gamma^2 = q^2 + j\omega\mu\sigma, \tag{B2}$$

Therefore, each in-plane Fourier mode satisfies an independent second-order ordinary differential equation, and its general solution is

$$\hat{\phi}(\mathbf{q}, z) = A(\mathbf{q})e^{-\Gamma z} + B(\mathbf{q})e^{\Gamma z}. \tag{B3}$$

Just Accepted

The corresponding normal current density is

$$\hat{J}_z(\mathbf{q},z) = -\frac{\sigma q^2}{\Gamma^2}\frac{\partial\hat{\phi}}{\partial z} = \frac{\sigma q^2}{\Gamma^2}\left[A(\mathbf{q})e^{-\Gamma z} - B(\mathbf{q})e^{\Gamma z}\right], \tag{B4}$$

at the surface $z=0$, we define $\hat{\phi}_s(\mathbf{q}) = \hat{\phi}(\mathbf{q},0)$, $\hat{J}_s(\mathbf{q}) = \hat{J}_z(\mathbf{q},0)$, and relate them through the surface impedance kernel $\hat{K}$:

$$\hat{\phi}_s(\mathbf{q}) = \hat{K}(\mathbf{q},\omega)\hat{J}_s(\mathbf{q}). \tag{B5}$$

B.2 Semi-Infinite Conductor

For a semi-infinite conductor occupying $z>0$, the field must decay as $z\to+\infty$. Therefore, $B(\mathbf{q})=0$. It follows that

$$\hat{\phi}_s = A(\mathbf{q}), \qquad \hat{J}_s = \frac{\sigma q^2}{\Gamma}A(\mathbf{q}). \tag{B6}$$

Substituting these expressions into (B5) gives

$$\hat{K}(\mathbf{q},\omega) = \frac{\Gamma}{\sigma q^2}, \tag{B7}$$

For convenience, we introduce the characteristic surface impedance

$$Z_c(\mathbf{q},\omega) = \frac{\Gamma}{\sigma q^2}. \tag{B8}$$

Then (B6) can be written in the compact form $\hat{K} = Z_c$.

B.3 Finite Thickness and Backside Boundary Conditions

We now consider a single conducting layer of thickness *h* that extends inward from the interface *z*=0. Its general solution remains that in (B3). If the backside is grounded, then $\hat{\phi}(\mathbf{q},h)=0$. Substituting this condition into (B3) gives

$$Ae^{-\Gamma h} + Be^{\Gamma h} = 0 \quad B = -Ae^{-2\Gamma h}, \tag{B9}$$

Therefore, $\hat{\phi}_s = A(1\,|\,e^{-2\Gamma h}), \quad \hat{J}_s = \frac{\sigma q^2}{\Gamma}A(1\,|\,e^{-2\Gamma h})$.

Hence, the input kernel is

Just Accepted

$$\hat{K} = \frac{\Gamma(1-e^{-2\Gamma h})}{\sigma q^2 (1+e^{-2\Gamma h})} = \frac{\Gamma \tanh(\Gamma h)}{\sigma q^2}, \tag{B10}$$

That is, $\hat{K} = Z_c \tanh(\Gamma h)$.

If the backside is insulated, the normal current vanishes at $z = h$, that is,

$$\hat{J}_z(\mathbf{q}, h) = 0 \quad \Leftrightarrow \quad \frac{\partial \hat{\phi}}{\partial z}|_{z=h} = 0, \tag{B11}$$

From (B4), we obtain

$$Ae^{-\Gamma h} - Be^{\Gamma h} = 0 \quad B = Ae^{-2\Gamma h}, \tag{B12}$$

Therefore,

$$\hat{\phi}_s = A(1 | e^{-2\Gamma h}), \quad \hat{J}_s = \frac{\sigma q^2}{\Gamma} A(1 | e^{-2\Gamma h}), \tag{B13}$$

Hence,

$$\hat{K} = \frac{\Gamma(1+e^{-2\Gamma h})}{\sigma q^2 (1-e^{-2\Gamma h})} = \frac{\Gamma \coth(\Gamma h)}{\sigma q^2}. \tag{B14}$$

That is, $\hat{K} = Z_c \coth(\Gamma h)$.

Equations (B6)–(B8) are the three standard single-layer kernels used in the main text.

B.4 Uniform Thin Film and Multilayer Recursion

If the substrate surface is covered by a uniform thin film with thickness t_f, complex conductivity σ_f, and permeability μ_f, then the corresponding propagation factor is

$$\Gamma_f = \sqrt{q^2 + j\omega\mu_f \sigma_f}, \quad Z_{c,f} = \frac{\Gamma_f}{\sigma_f q^2}, \tag{B15}$$

Let K_{load} denote the input impedance presented to this layer by the remaining structure beneath the film. Then, according to the standard transmission-line matching

Just Accepted

relation, the input kernel at the top surface of the film is

$$\hat{K}_{\text{in}} = Z_{c,f} \frac{K_{\text{load}} + Z_{c,f} \tanh(\Gamma_f t_f)}{Z_{c,f} + K_{\text{load}} \tanh(\Gamma_f t_f)}. \tag{B16}$$

For a multilayer structure, equation (B9) can be applied repeatedly in an upward recursion starting from the deepest layer.

For the two-body contact problem considered in this paper, the same normal interfacial current passes continuously through the materials on both sides, while the total surface potential drop equals the sum of the contributions from the two sides. Therefore, the total effective kernel is the series sum:

$$\hat{K}_{\text{eff}}(\mathbf{q}, \omega) = \hat{K}_{\text{in},1}(\mathbf{q}, \omega) + \hat{K}_{\text{in},2}(\mathbf{q}, \omega). \tag{B17}$$

B.5 Matrix-Free Discrete Operator Based on Zero Padding

In the numerical implementation, the physical computational domain is discretized on an $N \times N$ grid. To reduce periodic image interactions, the field is embedded in a larger extended domain, with $N_{\text{pad}} = \eta N, L_{\text{pad}} = \eta L, \eta \geq 1$. The field is set to zero outside the physical window. The discrete wave numbers on the extended domain are

$$q_x = \frac{2\pi k_x}{L_{\text{pad}}}, \qquad q_y = \frac{2\pi k_y}{L_{\text{pad}}}, \qquad q = \sqrt{q_x^2 + q_y^2}, \tag{B18}$$

Here, k_x and k_y are the FFT frequency indices.

Let P denote the projection operator onto the contact domain, and let $P^{\bullet}$ denote the embedding operator that maps the contact-domain variables back to the full grid. For the nonzero spectral modes, the matrix-free operator acting on the contact current vector $\mathbf{j}$ is written as

$$\mathsf{A}_{>0}(\mathbf{j}) = P\mathsf{F}^{-1}\left[\hat{K}_{\text{eff}}^{>0}\mathsf{F}(P^{\bullet}\mathbf{j})\right]. \tag{B19}$$

Just Accepted

where $\hat{K}_{\mathrm{eff}}^{>0}$ denotes the surface-impedance kernel for $q > 0$, with the discrete $q = 0$ entry set to zero.

The spatially uniform $q = 0$ component is treated separately and is not obtained by extrapolating the TM kernel to $q = 0$. For a same-surface source–return configuration, current conservation requires

$$\sum_{m,n} j_{mn} = 0. \tag{B20}$$

so that no separate zero-mode impedance is required.

For a finite grounded stack carrying a nonzero mean through-thickness current, the zero-mode area impedance is

$$K_0(\omega) = \sum_{l} \frac{h_l}{\sigma_l}, \tag{B21}$$

which, for a substrate covered by a uniform film, becomes

$$K_0(\omega) = \frac{h_{\mathrm{sub}}}{\sigma_{\mathrm{sub}}} + \frac{t_f}{\sigma_f}. \tag{B22}$$

The complete operator is then

$$\mathsf{A}(\mathbf{j}) = \mathsf{A}_{>0}(\mathbf{j}) + K_0 \bar{j} \mathbf{1}_c, \qquad \bar{j} = \frac{1}{N^2} \sum_{m,n} j_{mn}, \tag{B23}$$

where $\mathbf{1}_c$ denotes a uniform value on the contact-domain degrees of freedom. The zero-mode contribution is applied separately from the padded FFT operator and is therefore independent of the padding size.

A nonzero through-thickness zero mode is used only for a finite grounded stack. For a half-space or an insulated backside, a nonzero net current requires an explicitly specified remote return path and is not determined by the local TM kernel alone. The resulting linear system is solved iteratively in a Krylov subspace without explicitly

Just Accepted

assembling the corresponding dense matrix.

Appendix C. Variational Bounds and Discrete Closure for Gap Capacitance

C.1 Lower and Upper Bounds for Rough Surfaces Separated by a Gap

Consider two rough conducting surfaces described by $z = h_1(\mathbf{r})$ and $z = h_2(\mathbf{r})$, respectively, where $\mathbf{r} = (x, y) \in \Omega$, and let $g(\mathbf{r}) = h_2(\mathbf{r}) - h_1(\mathbf{r}) > 0$.

The dielectric region is

$$\mathsf{D} = \{(\mathbf{r}, z) : \mathbf{r} \in \Omega,\ h_1(\mathbf{r}) < z < h_2(\mathbf{r})\}, \tag{C1}$$

Set the electric potential on the lower surface to $\phi = 0$, and that on the upper surface to $\phi = V$. If the lateral boundary is insulating or periodic, the electrostatic energy is

$$W = \frac{\varepsilon}{2}\int_{\mathsf{D}} |\nabla \phi|^2 dV = \frac{1}{2} C V^2, \tag{C2}$$

Here, C denotes the exact capacitance of the rough gap.

Let $\mathbf{D}_t$ be any trial electric displacement field that is divergence-free and satisfies the no-flux condition on the lateral boundary. Choose a convenient vertical trial field

$$\mathbf{D}_t(\mathbf{r}, z) = \frac{\varepsilon V}{g(\mathbf{r})}\mathbf{e}_z. \tag{C3}$$

Since $\mathbf{D}_t$ is independent of z, one has $\nabla \cdot \mathbf{D}_t = 0$ in D. The flux through the upper surface is

$$Q_t = \int_{S_2} \mathbf{D}_t \cdot \mathbf{n} dS = \varepsilon V \int_{\Omega} \frac{1}{g(\mathbf{r})} dA, \tag{C4}$$

where the geometric identity $n_z dS = dA$ is used. The corresponding complementary energy is

$$\frac{1}{2\varepsilon}\int_{\mathsf{D}} |\mathbf{D}_t|^2 dV = \frac{\varepsilon V^2}{2}\int_{\Omega} \frac{1}{g(\mathbf{r})} dA, \tag{C5}$$

Just Accepted

Therefore, the Thomson variational principle gives

$$C \geq C_{\mathrm{L}} = \varepsilon \int_{\Omega} \frac{1}{g(\mathbf{r})} dA, \tag{C6}$$

Equation (C6) is exactly the local parallel-plate formula. Therefore, the commonly used local parallel-plate estimate for the capacitance is more appropriately interpreted as a lower bound rather than a strictly exact value.

Furthermore, by the Cauchy-Schwarz inequality,

$$\left(\int_{\Omega} 1 \, dA \right)^2 \leq \left(\int_{\Omega} g \, dA \right) \left(\int_{\Omega} \frac{dA}{g} \right), \tag{C7}$$

A cruder estimate is then

$$C \geq \varepsilon \frac{|\Omega|^2}{\int_{\Omega} g(\mathbf{r}) dA}, \tag{C8}$$

Next, an upper bound is derived from the Dirichlet principle. Choose the trial potential

$$\phi_t(\mathbf{r}, z) = V \frac{z - h_1(\mathbf{r})}{g(\mathbf{r})}, \tag{C9}$$

Introduce

$$\xi = \frac{z - h_1(\mathbf{r})}{g(\mathbf{r})} \in [0,1], \tag{C10}$$

Then

$$\nabla \phi_t = \frac{V}{g} \left[\mathbf{e}_z - (1 - \xi) \nabla h_1 - \xi \nabla h_2 \right], \tag{C11}$$

Accordingly,

$$\left| \nabla \phi_t \right|^2 = \frac{V^2}{g^2} \left\{ 1 + \left| (1 - \xi) \nabla h_1 + \xi \nabla h_2 \right|^2 \right\}, \tag{C12}$$

Integrating over $z \in [h_1, h_2]$ gives

Just Accepted

$$\int_{h_1}^{h_2} |\nabla \phi_t|^2 dz = \frac{V^2}{g}\left[1+\frac{|\nabla h_1|^2+|\nabla h_2|^2+\nabla h_1\cdot\nabla h_2}{3}\right], \tag{C13}$$

Substituting Eq. (C11) into the Dirichlet energy yields

$$C \le C_{\mathrm{U}}^{\mathrm{lin}} = \varepsilon\int_{\Omega}\frac{1}{g(\mathbf{r})}\left[1+\frac{|\nabla h_1|^2+|\nabla h_2|^2+\nabla h_1\cdot\nabla h_2}{3}\right]dA, \tag{C14}$$

Since the extra term in the bracket is non-negative, Eq. (C12) is indeed an upper bound. Therefore, the capacitance between two rough surfaces separated by a gap satisfies

$$\varepsilon\int_{\Omega}\frac{dA}{g(\mathbf{r})} \le C \le \varepsilon\int_{\Omega}\frac{dA}{g(\mathbf{r})}+\frac{\varepsilon}{3}\int_{\Omega}\frac{|\nabla h_1|^2+|\nabla h_2|^2+\nabla h_1\cdot\nabla h_2}{g(\mathbf{r})}dA. \tag{C15}$$

C.2 Contact, Physical Cutoff, and Effective Gap

For contact problems, the mechanical gap may approach zero over part of the domain. Let $g_{\mathrm{m}}(\mathbf{r}) \ge 0$ denote the mechanical gap computed by the mechanical solver. To account for the effect of a dielectric film or any equivalent series thickness, define the effective gap as

$$G(\mathbf{r}) = g_m(\mathbf{r}) + t_s, \tag{C16}$$

Here, t_s is the equivalent series thickness. For a uniform film with thickness t_f and relative permittivity $\varepsilon_{r,f}$, one naturally takes

$$t_s = \frac{t_f}{\varepsilon_{r,f}}. \tag{C17}$$

When $G(\mathbf{r}) \to 0$, the purely geometric capacitance integral diverges. To regularize the near-contact divergence in a physically meaningful way, introduce a minimum effective gap

$$G_\tau(\mathbf{r}) = \max\{G(\mathbf{r}), \tau\} = \max\left\{g_{\mathrm{m}}(\mathbf{r}) + t_s, \tau\right\}, \tag{C18}$$

where $\tau > 0$ denotes an effective cutoff associated with breakdown, tunneling, finite

Just Accepted

film thickness, unresolved microscale roughness, or numerical resolution.

Accordingly, the capacitive branch is defined over the non-contact dielectric region $\Omega_{\mathrm{nc}} = \Omega$, Ω_{c}.. In practical computations, Ω_{nc} is usually given equivalently by the complement of the true contact mask. Under the above regularization, the capacitive admittance is written as

$$Y_{gap} = j\omega C_{gap}, \tag{C19}$$

Its rigorous lower bound is still provided by the Thomson construction:

$$C_{\mathrm{gap}} \geq C_{\mathrm{L},\tau} = \varepsilon \int_{\Omega_{\mathrm{nc}}} \frac{1}{G_{\tau}(\mathbf{r})} dA. \tag{C20}$$

Conversely, once true contact is allowed, there is usually no finite upper bound that depends only on the unregularized mechanical gap. This is because a region with positive area can approach the opposing conductor arbitrarily closely. The capacitance can then become arbitrarily large. Therefore, in the presence of contact, any finite upper bound must explicitly involve a positive minimum gap, such as G_{τ}, or another physical regularization.

With the same linear trial potential as in Section C.1, the corresponding regularized upper bound is

$$C_{\mathrm{gap}} \leq C_{\mathrm{U},\tau}^{\mathrm{lin}} = \varepsilon \int_{\Omega_{\mathrm{nc}}} \frac{1}{G_{\tau}(\mathbf{r})} \left[1 + \frac{|\nabla h_1|^2 + |\nabla h_2|^2 + \nabla h_1 \cdot \nabla h_2}{3} \right] dA, \tag{C21}$$

Thus, for the regularized gap problem,

$$C_{\mathrm{L},\tau} \leq C_{\mathrm{gap}} \leq C_{\mathrm{U},\tau}^{\mathrm{lin}}, \tag{C22}$$

In the special case $h_1 = 0$, $h_2 = G(\mathbf{r})$, and $|\nabla G| = 1$, Eq. (C19) reduces to the derivative-expansion correction C; $\grave{o}\int G^{-1}(1+|\nabla G|^2/3)dA$ reported by Fosco et al.

Just Accepted

[27] for electrostatic PFA. The present derivation differs in purpose: it is based on the Dirichlet principle and is used here as a computable upper estimate for a regularized non-contact gap in a load-dependent rough-contact problem.

C.3 Discrete Closure Used in the Numerical Implementation

For the configuration used in the numerical implementation of this work, a rigid rough surface faces a deformable smooth substrate. The mechanical deformation of the substrate is included in g_{m}. In the slope correction of the capacitive closure, only the prescribed rough surface height $h(\mathbf{r})$ is retained.

The implemented capacitance is taken as the midpoint of the regularized lower and upper bounds. This gives the following discrete closure:

$$C_{\mathrm{gap}}^{\mathrm{num}} = \varepsilon_0 \sum_{(m,n)\in\Omega_{\mathrm{nc}}} \left[\frac{1}{G_{\tau,mn}} + \frac{|\nabla h|_{mn}^2}{6G_{\tau,mn}} \right] \Delta x \Delta y, \tag{C23}$$

where

$$G_{\tau,mn} = \max\left\{ g_{\mathrm{m},mn} + \frac{t_f}{\varepsilon_{r,f}}, \tau \right\}, \tag{C24}$$

where $g_{\mathrm{m},mn}$ is the mechanical gap at grid point (m,n), and h is the rough surface height field. The surface gradient correction term is computed by a spectral method:

$$\hat{\partial_x} h = iq_x \hat{h}, \quad \hat{\partial_y} h = iq_y \hat{h}, \tag{C25}$$

Therefore,

$$|\nabla h|^2 = (\partial_x h)^2 + (\partial_y h)^2, \tag{C26}$$

Equation (C21) should be viewed as an approximate closure adopted in this work. It plays two roles. First, it provides a directly computable capacitive branch that is

Just Accepted

explicitly coupled to the mechanical gap field. Second, it makes explicit the effects of the effective cutoff $G_{\tau,mn}$ and the local slope correction on the result. This helps clarify the relation between this approximation and the rigorous variational bounds given by Eqs. (C18)–(C20).

In the main text, $C_{\mathrm{gap}}^{\mathrm{num}}$ is denoted simply by C_{gap}. Finally, after the conductive branch is solved, the total interfacial admittance is written as

$$Y_{tot} = Y_{cond} + j\omega C_{gap}, \tag{C27}$$

Equivalently,

$$Z_{\mathrm{tot}} = \frac{1}{Y_{\mathrm{cond}} + j\omega C_{\mathrm{gap}}}, \tag{C28}$$

This is the parallel form used in the main text.

Declaration of interests

The authors declare that they have no known competing financial interests or personal relationships that could have appeared to influence the work reported in this paper.

Acknowledgements

The authors gratefully acknowledge support from the National Natural Science Foundation of China (grant numbers 12272157 and 12327901), the Natural Science Foundation for Key Program of Gansu Province (grant number 24JRRA782), and the Fundamental Research Funds for the Central Universities (grant number lzujbky-2023-ey05).

Data availability

The data generated and analyzed during this study, including the numerical results

Just Accepted

used to produce the figures, are available from the corresponding authors upon reasonable request.

References

[1] S.V. Angadi, R.L. Jackson, V. Pujar, M.R. Tushar, A comprehensive review of the finite element modeling of electrical connectors including their contacts, IEEE Trans. Compon. Packag. Manuf. Technol. 10 (2020) 836–844. https://doi.org/10.1109/TCPMT.2020.2982207

[2] J. Song, A. Shukla, R. Probst, The state of health of electrical connectors, Machines 12 (2024) 474. https://doi.org/10.3390/machines12070474

[3] Y. Sui, P. Xing, G. Li, H. Zhang, W. Wang, H. Zhang, Theoretical modeling and numerical simulation of current-carrying friction and wear: State of the art and challenges, Lubricants 13 (2025) 370. https://doi.org/10.3390/lubricants13080370

[4] R.S. Timsit, High speed electronic connector design: A review of electrical and electromagnetic properties of passive contact elements -- Part 1, IEICE Trans. Electron. E91-C (2008) 1178–1191. https://doi.org/10.1093/ietele/e91-c.8.1178

[5] Y. Zhou, J. Gao, T. Zhang, J. Lei, Thermal behavior of plated electrical connectors under high-power and high-frequency excitation, Electronics 14 (2025) 2353. https://doi.org/10.3390/electronics14122353

[6] Y. Zhou, T. Zhang, G. Xie, J. Gao, The effect of scratch-induced microscale surface roughness on signal transmission in radio frequency coaxial connectors, Micromachines 16 (2025) 837. https://doi.org/10.3390/mi16080837

[7] A.W. Bush, R.D. Gibson, T.R. Thomas, The elastic contact of a rough surface, Wear 35 (1975) 87–111. https://doi.org/10.1016/0043-1648(75)90145-3

[8] J.A. Greenwood, J.B.P. Williamson, Contact of nominally flat surfaces, Proc. R. Soc. Lond. Ser. Math. Phys. Sci. 295 (1966) 300–319. https://doi.org/10.1098/rspa.1966.0242

[9] R. Holm, Electric Contacts: Theory and Application, fourth ed., Springer-Verlag, Berlin, 1967. https://doi.org/10.1007/978-3-662-06688-1.

[10] B.N.J. Persson, Relation between interfacial separation and load: A general theory of contact mechanics, Phys. Rev. Lett. 99 (2007) 125502. https://doi.org/10.1103/PhysRevLett.99.125502

[11] A. Dayan, Y. Huang, A. Schuchinsky, Passive intermodulation at contacts of rough conductors, Electron. Mater. 3 (2022) 65–81. https://doi.org/10.3390/electronicmat3010007

[12] X. Wang, C. Zhai, Y. Gan, Stress-dependent electrical impedance behaviours at fractal rough interfaces, Surf. Topogr. Metrol. Prop. 9 (2021) 025014. https://doi.org/10.1088/2051-672X/abf84f

[13] C. Zhai, D. Hanaor, G. Proust, L. Brassart, Y. Gan, Interfacial electro-mechanical behaviour at rough surfaces, Extreme Mech. Lett. 9 (2016) 422–429. https://doi.org/10.1016/j.eml.2016.03.021

[14] B.N.J. Persson, Contact mechanics for randomly rough surfaces, Surf. Sci. Rep. 61 (2006) 201–227. https://doi.org/10.1016/j.surfrep.2006.04.001

[15] V.A. Yastrebov, G. Anciaux, J.-F. Molinari, From infinitesimal to full contact between rough surfaces: Evolution of the contact area, Int. J. Solids Struct. 52 (2015) 83–102.

JUST Accepted

https://doi.org/10.1016/j.ijsolstr.2014.09.019
[16] S. Timsit, Electrical contact resistance: Properties of stationary interfaces, in: Electrical Contacts - 1998. Proceedings of the Forty-Fourth IEEE Holm Conference on Electrical Contacts (Cat. No.98CB36238), IEEE, Arlington, VA, USA, 1998, pp. 1–19. https://doi.org/10.1109/HOLM.1998.722422
[17] J.R. Barber, Incremental stiffness and electrical contact conductance in the contact of rough finite bodies, Phys. Rev. E 87 (2013) 013203. https://doi.org/10.1103/PhysRevE.87.013203
[18] J.R. Barber, Bounds on the electrical resistance between contacting elastic rough bodies, Proc. R. Soc. Lond. Ser. Math. Phys. Eng. Sci. 459 (2003) 53–66. https://doi.org/10.1098/rspa.2002.1038
[19] V.A. Yastrebov, G. Anciaux, J.-F. Molinari, Contact between representative rough surfaces, Phys. Rev. E 86 (2012) 035601. https://doi.org/10.1103/PhysRevE.86.035601
[20] V.A. Yastrebov, G. Cailletaud, H. Proudhon, F.S.M. Mballa, S. Noel, P. Teste, F. Houze, Three-level multi-scale modeling of electrical contacts sensitivity study and experimental validation, in: 2015 IEEE 61st Holm Conference on Electrical Contacts (Holm), IEEE, San Diego, CA, USA, 2015, pp. 414–422. https://doi.org/10.1109/HOLM.2015.7355130
[21] R.L. Jackson, E.R. Crandall, M.J. Bozack, Rough surface electrical contact resistance considering scale dependent properties and quantum effects, J. Appl. Phys. 117 (2015) 195101. https://doi.org/10.1063/1.4921110
[22] Y.-H. Li, L.-L. Ke, G.-G. Chang, M.A. Güler, F. Shen, On the electrical contact resistance model of rough surfaces based on multi-physics modeling, Int. J. Solids Struct. 321 (2025) 113583. https://doi.org/10.1016/j.ijsolstr.2025.113583
[23] Y.-H. Li, F. Shen, M.A. Güler, L.-L. Ke, Modeling multi-physics electrical contact on rough surfaces considering elastic-plastic deformation, Int. J. Mech. Sci. 269 (2024) 109066. https://doi.org/10.1016/j.ijmecsci.2024.109066
[24] Y.-H. Li, F. Shen, M.A. Güler, L.-L. Ke, A rough surface electrical contact model considering the interaction between asperities, Tribol. Int. 190 (2023) 109044. https://doi.org/10.1016/j.triboint.2023.109044
[25] Y.-P. Zhao, G.-C. Wang, T.-M. Lu, G. Palasantzas, J.Th.M. De Hosson, Surface-roughness effect on capacitance and leakage current of an insulating film, Phys. Rev. B 60 (1999) 9157–9164. https://doi.org/10.1103/PhysRevB.60.9157
[26] N.C. Bruce, A. García-Valenzuela, D. Kouznetsov, Rough-surface capacitor: Approximations of the capacitance with elementary functions, J. Phys. Appl. Phys. 32 (1999) 2692–2702. https://doi.org/10.1088/0022-3727/32/20/317
[27] C.D. Fosco, F.C. Lombardo, F.D. Mazzitelli, An improved proximity force approximation for electrostatics, Ann. Phys. 327 (2012) 2050–2059. https://doi.org/10.1016/j.aop.2012.04.006
[28] S. Torabi, M. Cherry, E.A. Duijnstee, V.M. Le Corre, L. Qiu, J.C. Hummelen, G. Palasantzas, L.J.A. Koster, Rough electrode creates excess capacitance in thin-film capacitors, ACS Appl. Mater. Interfaces 9 (2017) 27290–27297. https://doi.org/10.1021/acsami.7b06451
[29] Y. Xu, Y. Wu, R.L. Jackson, Electrical contact with dielectric breakdown of interfacial gap, J. Tribol. 147 (2025) 051109. https://doi.org/10.1115/1.4067373
[30] Y. Xu, N. Morris, Y. Wu, Electrified EHL line contact with dielectric breakdown of lubricant — A numerical model, Tribol. Int. 217 (2026) 110901. https://doi.org/10.1016/j.triboint.2025.110901
Just Accepted

[31] X. Wang, Q.J. Wang, C. Davies, A. Mo, S. Liu, N. Ren, Surface asperity-enhanced micro electrical discharge in lubricated contact interfaces, Tribol. Int. 209 (2025) 110742. https://doi.org/10.1016/j.triboint.2025.110742

[32] L. Frérot, G. Anciaux, V. Rey, S. Pham-Ba, J.-F. Molinari, Tamaas: A library for elastic-plastic contact of periodic rough surfaces, J. Open Source Softw. 5 (2020) 2121. https://doi.org/10.21105/joss.02121

[33] S. Liu, Q. Wang, G. Liu, A versatile method of discrete convolution and FFT (DC-FFT) for contact analyses, Wear 243 (2000) 101–111. https://doi.org/10.1016/S0043-1648(00)00427-0

[34] N. Bowler, Analytical solution for the electric field in a half-space conductor due to alternating current injected at the surface, *J. Appl. Phys.* 95 (2004) 344–348.https://doi.org/10.1063/1.1630700

[35] W. Ta, S. Qiu, Y. Wang, J. Yuan, Y. Gao, Y. Zhou, Volumetric contact theory to electrical contact between random rough surfaces, Tribol. Int. 160 (2021) 107007. https://doi.org/10.1016/j.triboint.2021.107007

[36] H. Zhao, W. Ta, Y. Zhou, The mechanical-thermal-electrical contact behaviors between rough surfaces under cyclic loading, Acta Mech. Sin. 39 (2023) 123212. https://doi.org/10.1007/s10409-023-23212-x

[37] C. Zhai, D. Hanaor, Y. Gan, Contact stiffness of multiscale surfaces by truncation analysis, Int. J. Mech. Sci. 131–132 (2017) 305–316. https://doi.org/10.1016/j.ijmecsci.2017.07.018

[38] Y.-K. An, H. Sohn, Integrated impedance and guided wave based damage detection, Mechanical Systems and Signal Processing 28 (2012) 50–62. https://doi.org/10.1016/j.ymssp.2011.11.016

[39] G. Li, M. Luo, J. Huang, W. Li, Early-age concrete strength monitoring using smart aggregate based on electromechanical impedance and machine learning, Mechanical Systems and Signal Processing 186 (2023) 109865. https://doi.org/10.1016/j.ymssp.2022.109865

[40] L. Frérot, M. Bonnet, J.-F. Molinari, G. Anciaux, A Fourier-accelerated volume integral method for elastoplastic contact, Computer Methods in Applied Mechanics and Engineering 351 (2019) 951–976. https://doi.org/10.1016/j.cma.2019.04.006

[41] A. Tiwari, A. Almqvist, B.N.J. Persson, Plastic deformation of rough metallic surfaces, Tribology Letters 68 (2020) 129. https://doi.org/10.1007/s11249-020-01368-9

Just Accepted



Wurui Ta. He received his Ph.D degrees in college of civil engineering and mechanics of Lanzhou University, China, in 2016. He is the deputy dean of the Department of mechanics and Engineering Sciences. His research areas cover the superconducting electromagnetic solid mechanics and contact friction mechanics.



Aizhong Liao. He has been studying for a master's degree in college of civil engineering and mechanics of Lanzhou University since 2025, and his research

focuses on contact mechanics and electrical contacts.

Just Accepted